

DOI:10.1002/ejic.201403013

Mononuclear Iron(II) Dicarbonyls Derived from NNS Ligands – Structural Models Related to a “Pre-Acyl” Active Site of Mono-Iron (Hmd) Hydrogenase

Keren A. Thomas Muthiah,^[a] Gummadi Durgaprasad,^[a]
Zhu-Lin Xie,^[a] Owen M. Williams,^[a] Christopher Joseph,^[a]
Vincent M. Lynch,^[a] and Michael J. Rose*^[a]

Keywords: Iron / Carbonyl ligands / Enzymes / Hydrogenase / Photolysis / Schiff bases

We report the syntheses and characterization of dicarbonyliron complexes derived from tridentate, *ortho*-substituted Schiff base pyridine/thioether ligands (_RNNS). Metalation reactions of _RNNS (R = CH₃, OCH₃) at low temperature (−78 °C) with [Fe(CO)₄(Br)₂] afforded the desired complexes [(_RNNS)-Fe(CO)₂Br]₂ (**2**-CO_{Br}, **3**-CO_{Br}). Reactions under similar conditions with more sterically demanding ligands [R = quinoline (Q), ClPh] afforded complex salts of the form [(_RNNS)-Fe(CO)₂Br][Fe(CO)₃(Br)₃] (**4**-CO_{Fe} and **5**-CO_{Fe}, respectively). Alternatively, the metalation of the _RNNS ligands (for all R ≠ H) with [Fe(CO)₄(Br)₂] in Et₂O at room temperature reliably affords the complex species of type [(_RNNS)Fe(CO)₂Br][Fe(CO)₃(Br)₃] (**2**-CO_{Fe}, **3**-CO_{Fe}, **5**-CO_{Fe}). The metalation reactions of _RNNS at only moderately low temperatures (−20 to 0 °C) result in the loss of CO to form the corresponding trigonal-bipyramidal iron(II) dibromide species of type [(_RNNS)-FeBr₂] (**2**-Br, **4**-Br, **5**-Br; μ_{eff} ≈ 5.3 μ_B, S = 2). The IR spectrum

of each dicarbonyl cation exhibits two ν(CO) stretches at $\tilde{\nu} \approx 2070$ and 2030 cm^{−1}. Low-temperature ¹H NMR spectroscopy measurements of **2**-CO to **5**-CO in CD₃CN (−35 to 5 °C) revealed sharp resonances in the diamagnetic region. Under dark conditions, each dicarbonyl species is relatively stable (<10 % loss of CO, 1–2 h). However, photolysis revealed varying extents of photostability (stability rank: R = OMe > Me ≈ Q > ClPh). An examination of the structural parameters reveals that higher photostabilities correlate with shorter Fe–C(O) bond lengths, which are induced by variation of the *ortho* substituent of the pyridine ring. DFT calculations along the putative photolysis pathway revealed that the bulky ligand substituent (in **5**-CO) destabilizes the monocarbonyl intermediate, and this is a likely explanation for its more rapid rate of CO photodissociation. Relevance to a possible “apo-active site” of mono-iron hydrogenase (pre-acyl formation) is discussed.

Introduction

Hydrogenases are enzymes that generate or utilize dihydrogen (H₂) and can be found in both bacteria and archaea. Owing to the reliance of such microorganisms on the natural abundance of elements, the enzymes utilize only biologically available metal ions, most notably iron and nickel. There are three known types of hydrogenases, [NiFe]-, [FeFe]-, and the most recently discovered mono-[Fe]-hydrogenase, also known as the dihydrogen-forming methylenetetrahydromethanopterin dehydrogenase (Hmd).^[1,2] Mono-[Fe] H₂ase is endogenously expressed in some strains of methanobacter such as *Methanocaldococcus jannaschii* (known enzyme X-ray structure), *Methanothermobacter marburgensis*, and *Methanobrevibacter smithii*. Notably, the enzyme is only significantly expressed under nickel-limiting conditions; otherwise, [NiFe]-hydrogenase is

responsible for the utilization of H₂ under physiological conditions. Overall, these enzymes have been proposed to serve as inspiration for the synthesis of base-metal complexes that could replace platinum, iridium, and rhodium complexes in catalytic processes.

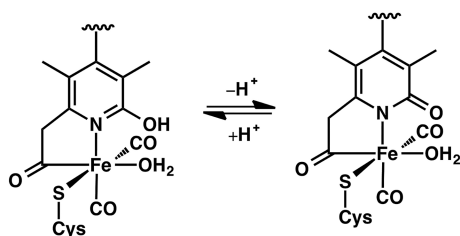
In contrast to the better-studied [NiFe]- and [FeFe]-hydrogenases, [Fe]-H₂ase is not a redox enzyme: it contains no iron–sulfur electron transport system and, to date, only the Fe^{II} oxidation state has been observed in active preparations. Not surprisingly, the active site of Hmd is unique in biological systems, as it splits molecular hydrogen, despite the proposition that the metal center is redox-inactive. The enzyme performs the heterolytic cleavage of H₂, followed by a hydride transfer to methylenetetrahydromethanopterin (H₄MPT⁺) to form the reduced product methylene-H₄MPT. The methanopterin substrate acts as a C₁ carrier in a methanogenic CO₂ fixation pathway. Thus, [Fe]-hydrogenase performs one of the key steps in the reduction of carbon dioxide to methane.^[1,2]

As shown in Scheme 1, the active site consists of one Fe^{II} center ligated to a bidentate 6-hydroxypyridylacyl moiety, two carbonyl ligands in *cis* orientation, the sulfur atom

[a] Department of Chemistry, The University of Texas at Austin, Austin, TX 78712, USA
E-mail: mrose@cm.utexas.edu
http://www.roseresearchgroup.org

Supporting information for this article is available on the WWW under <http://dx.doi.org/10.1002/ejic.201403013>.

from the Cys₁₇₆ residue, and the solvent/H₂ coordination site *trans* to the acyl unit. The iron–acyl unit is one of the distinctive features that sets the Hmd active site apart from all other known metalloprotein active sites. The mechanism responsible for the formation of this rare metal–carbon bond is still unknown.^[3,4] Recently, Shima and co-workers reported an elegant ¹³C-labeling study to trace the origin of the acyl/pyridone-containing Fe–GMP (GMP = guanosine monophosphate) cofactor.^[5] The highly substituted apopyridone/GMP cofactor could be constructed biosynthetically in autotrophic *M. marburgensis* and *M. smithii* from [¹³C]-acetate and ¹³CO₂ (through pyruvate → ketoallulose). The generated pyridone contains an *ortho*-(CH₂)CO₂H substituent (the acyl precursor), but the exact pathway for the reduction and/or decarboxylation of the acidic moiety remains unclear. Interestingly, growth under a ¹³CO atmosphere led to ¹³C labeling of both the metal-bound carbonyl (C≡O) ligands and the Fe–¹³C(=O)_{acyl} unit. Additionally, Hu and co-workers found that the incubation of a synthetic Fe–C(=O)_{acyl} complex with ¹³CO under select conditions (dark, several days; UV, hours) resulted in exchange to form a labeled Fe–¹³C(=O)_{acyl} unit.^[6] This suggests a plausible N-ligated methylpyridine or Fe–(CH₂)_{alkyl} intermediate during the exchange, wherein the acyl unit may be (re)-formed across an intermediate by an organometallic process.



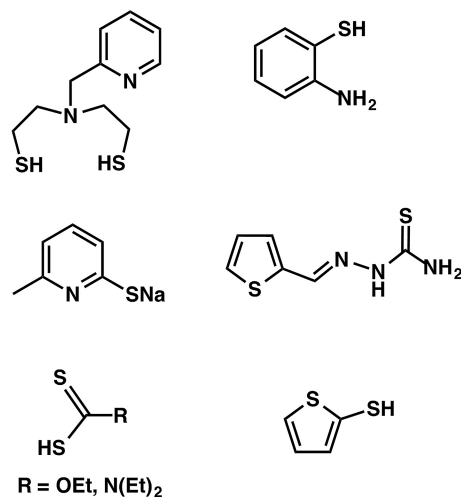
Scheme 1. The possible protonation states in the active site of [Fe]-hydrogenase.

In this work, we were interested to probe such a putative apo-active site (or intermediate thereof) before the formation of the acyl unit. Many recently reported model complexes utilize an Fe⁰ or Fe^{II} source (namely, [Fe(CO)₅] or Na₂[Fe(CO)₄], respectively) as the metalating agent, and this is the most efficient synthetic route to iron carbonyls containing an acylpyridyl unit.^[6–8] As we were interested in the isolation of apo/intermediate complexes without the acyl unit, Fe^{II} sources were most applicable. Additionally, the most likely biological source of iron carbonyl during the assembly of the active site is Fe^{II}. As such, we have utilized [Fe(CO)₄(X)₂] (X = Br, I), as reported by others.^[9–12] Several recent reports regarding the assembly of the [FeFe] H-cluster also provide inspiration for investigations regarding the biogenesis of the mono-[Fe] active site.^[13–16]

This research is focused on the utilization of biologically relevant ligands as found in the active site, such as N and S donors in addition to carbonyl ligands. That is, we wished to avoid phosphines, cyclopentadienyl (Cp) derivatives, carbenes, or carbanion-based pincer ligands to artificially

stabilize the *cis*-{Fe(CO)₂} moiety. Additionally, to highlight the structure and properties of a putative apo- or intermediate active site, we have avoided the use of an acyl ligand to stabilize the complex.

A close inspection of crystallographically characterized iron dicarbonyls reveals surprisingly few examples of mononuclear non-phosphine- and non-acyl-supported iron dicarbonyls. Of these select examples, several complexes possess nonbridging thiolates. For example, Pickett and co-workers reported an early structural mimic of [Fe]-H₂ase derived from the tetradentate (N₂S₂), pyridine-based dithiolate ligand shown below. The resulting complex exhibited a mononuclear Fe^{II} center ligated to *cis*-carbonyl ligands and the deprotonated dithiolate ligand.^[11] To prepare CO-releasing molecules (CORMs), Westerhausen synthesized a mononuclear iron carbonyl thiolate complex derived from 2 equiv. of aminothiophenol, formulated as [(L_{NS})₂Fe(CO)₂], which also featured the *cis*-dicarbonyl motif.^[17] Liaw reported the structure of a closely related complex derived from 1 equiv. of the same ligand, which generated [(L_{NS})-Fe{*cis*-(CO)₂}₂(CN)]⁻ as a five-coordinate species.^[18]



More prevalent, however, are other sulfur-bearing ligands such as thiocarbamates, xanthates, thioureas, thio-pyridines, and 2-thiopyridine (2TT). These ligands are less prone to promoting dimerization and, thus, have been used in mononuclear systems. For example, Hu reported a structural [Fe]-H₂ase model derived from 2-thiopyridine (pyS), namely, [(pyS)Fe{*cis*-(CO)₂}₂(CH₃CO)(CN)]⁻,^[10] whereas Liaw and co-workers structurally characterized the related complexes [(pyS)Fe{*cis*-(CO)₂}₂(*trans*-CN)₂]⁻ and [(pyS)₂Fe{*cis*-(CO)₂}₂]⁻.^[19,20] The thiophene-derived complex [(bpy)(2TT)₂Fe{*cis*-(CO)₂}₂] (bpy = 2,2'-bipyridine) was also reported.^[21] Mononuclear carbonyls such as [(EtOCS₂)Fe{*cis*-(CO)₂}₂(CN)₂]⁻ (xanthate) and [(Et₂NCS₂)Fe{*cis*-(CO)₂}₂(CN)₂]⁻ (carbamate) may also be reliably derived from thiocarboxylates.^[19] The thiourea-derived complex [(L_{NS})₂Fe{*cis*-(CO)₂}₂] is another closely related example.^[22]

However, an inspection of the structure database reveals no examples of Fe^{II} carbonyls derived from mixed N/S

donor sets containing a thioether motif; such a donor set would offer a different strategy to include sulfur donors and prevent dimerization. Thus, we devised a simple series of *ortho*-substituted Schiff base pyridine/thioether ligands [R NNS; R = Me, OMe, quinoline (Q), ClPh] to explore the importance of the *cis*-{Fe(CO) $_2$ } fragment. In this work, we present the synthetic routes, X-ray structures, and properties of iron(II) *cis*-carbonyls derived from a set of Schiff base pyridine/thioether ligands. We report the effects of light, temperature, and reaction conditions (solvent, stoichiometry, CO gas) in the preparation and characterization of the complexes.

Results and Discussion

Syntheses and Reactivity

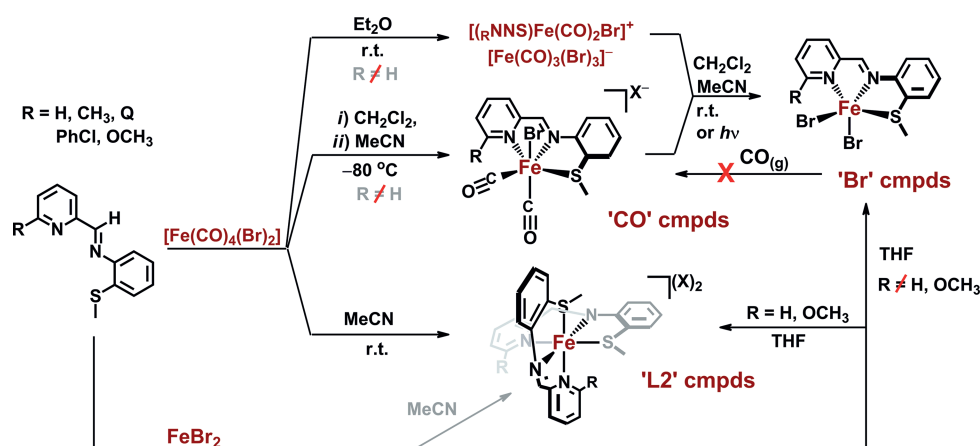
The NNS ligands used in this work were prepared from the condensations of *ortho*-substituted pyridinecarbaldehydes with 2-(methylthio)aniline in MeOH at room temperature or under mild reflux conditions. The iron carbonyl bromide starting salt [Fe(CO) $_4$ (Br) $_2$] was prepared by modification of a previously reported procedure.^[9] The overall synthetic and reactivity scheme is summarized in Scheme 2. The metalation of unsubstituted H NNS with [Fe(CO) $_4$ (Br) $_2$] was pursued initially in tetrahydrofuran (THF), CH $_2$ Cl $_2$, and MeCN under ambient conditions; this resulted in the formation of violet bisligated species of the type [(R NNS) $_2$ Fe](X) $_2$ as the only isolable product (as the Br $^-$ salt or the BF $_4^-$ salt after AgBF $_4$ treatment). We next attempted to prevent the loss of CO by performing the metalations at low temperature.

At low temperatures (-80 °C), the metalation of R NNS with [Fe(CO) $_4$ (Br) $_2$] in CH $_2$ Cl $_2$ afforded green solutions, which upon the addition of MeCN afforded bright orange products of the desired carbonyl complexes [(R NNS)Fe(CO) $_2$ Br]Br [R = CH $_3$ (2-CO $_{Fe}$), OCH $_3$ (3-CO $_{Fe}$)]. The addition of MeCN was required to isolate the desired com-

plex, presumably facilitating the dissociation of the bromide ions (poor leaving group in neat CH $_2$ Cl $_2$). The resulting bromide salts could be recrystallized at low temperatures from MeCN/Et $_2$ O or DMF/Et $_2$ O. Notably, 3-CO $_{Br}$ crystallizes as an H $_2$ O·MeCN solvate (even from DMF); therefore, it is stable to both coordinating and protic solvents. Thus, it appears that a temperature-dependent, dissociative mechanism is the main pathway of CO loss. Along the same lines, reaction or recrystallization attempts above -20 °C resulted in the loss of CO and the isolation of the corresponding green dibromide species [(R NNS)Fe(Br) $_2$] in all cases. Notably, the isolation of the bromide salts was exclusive to the Me NNS and OMe NNS ligands. For example, under the same metalation conditions (CH $_2$ Cl $_2$ /MeCN, low temperature), reactions with the bulkier Q NNS ligand afforded the same cation, but it was instead paired with a complex anion in the form [(Q NNS)Fe(CO) $_2$ Br][Fe(CO) $_3$ (Br) $_3$] (4-CO $_{Fe}$). The reasons for this are discussed further below.

The same NNS-ligated iron carbonyl cations could also be prepared at room temperature by the reactions of R NNS with [Fe(CO) $_4$ (Br) $_2$] in Et $_2$ O (both reactants soluble), which led to the immediate precipitation of the crude products. Recrystallization from MeCN/Et $_2$ O at -40 °C afforded orange to red crystalline samples of complex species of the type [(R NNS)Fe(CO) $_2$ Br][Fe(CO) $_3$ (Br) $_3$] [R = CH $_3$ (2-CO $_{Fe}$), OCH $_3$ (3-CO $_{Fe}$), and Q (4-CO $_{Fe}$)]. One exception was that the recrystallization of [(ClPhNNS)Fe(CO) $_2$ Br][Fe(CO) $_3$ (Br) $_3$] from MeCN/Et $_2$ O was especially slow (2–4 weeks) and afforded a different complex salt, namely, [(ClPhNNS)Fe(CO) $_2$ Br][Fe(Br) $_4$] (5-CO $_{FeBr}$). No carbonyl products were isolated for the simplest ligand with R = H.

In the context of other synthetic approaches, Darensbourg and co-workers performed metalations of monodentate ligands (carbenes, py, PPh $_3$) and bidentate ligands (bpy, 2-pyridone) with [Fe(CO) $_4$ I $_2$] in hexane at room temperature;^[23] no bisligated products were reported in these cases, except for PMe $_3$, which afforded the complex [Fe(CO) $_2$ (PMe $_3$) $_2$ I $_2$] under certain conditions. These researchers noted that dark conditions were required for the



Scheme 2. Synthetic pathways for iron species with R NNS (R = CH $_3$, OCH $_3$, Q, PhCl) ligands derived from metalation with [Fe(CO) $_4$ (Br) $_2$] or FeBr $_2$.

isolation of the complexes, and this is also an important point in this work (vide infra).^[9]

As we at first serendipitously obtained the dibromide species that resulted from the loss of CO from the carbonyl complexes, we subsequently independently synthesized these species in higher yields by the metalation of FeBr₂ with _RNNS in THF. A selection of ligands with bulky substituents (R = CH₃, Q, ClPh) afforded dark green solutions of the desired dibromide species (**2-Br**, **4-Br**, and **5-Br**, respectively). Crystallization from pentane or Et₂O vapor diffusion afforded single crystals of the products, which

ranged from brown to green and blue-green. The ligands with the least restrictive R groups (R = H, OCH₃) afforded only violet solutions of the bisligated dication, that is, [(_RNNS)₂Fe]²⁺. None of the isolated dibromide species could be converted into the corresponding carbonyl compounds under 1 atm of CO (−40 °C → room temp.), most likely because of the low affinity of the high-spin Fe^{II} center (*S* = 2, vide infra) for CO. The crystal data and refinement parameters for the carbonyl, dibromide, and bisligated complexes are summarized in (Table 1), and their structures will be discussed in the next section.

Table 1. Crystal data and refinement parameters for the carbonyl, dibromide, and bisligated complexes.

	2-CO_{Br}	3-CO_{Fe}	5-CO_{Fe}	2-Br
Formula	C ₁₈ H ₁₉ N ₃ O ₃ SBr ₂ Fe	C ₂₁ H ₁₇ Br ₄ Fe ₂ N ₄ O ₆ S	C ₂₁ H ₁₅ Br ₅ ClFe ₂ N ₂ O ₂ S	C ₁₄ H ₁₄ Br ₂ N ₂ S
FW	573.09	870.78	906.11	458.00
Color	orange	orange	red	brown
Habit	block	needle	needle	block
Size [mm]	0.25 × 0.18 × 0.11	0.23 × 0.08 × 0.04	0.08 × 0.005 × 0.002	0.32 × 0.25 × 0.20
<i>T</i> (K)	163(2)	153(2)	100(3)	163(2)
λ [Å]	0.71073	0.71073	0.77490	0.71073
Lattice	orthorhombic	triclinic	orthorhombic	monoclinic
Space group	<i>Pna</i> 2 ₁	<i>P</i> $\bar{1}$	<i>Fdd</i> 2	<i>P</i> 2 ₁ / <i>n</i>
<i>a</i> [Å]	13.133(3)	8.8332(3)	29.751(6)	11.794(4)
<i>b</i> [Å]	18.926(5)	13.5199(4)	36.638(7)	10.086(3)
<i>c</i> [Å]	8.738(2)	13.6379(5)	10.333(2)	13.714(5)
<i>a</i> [°]	90	114.510(2)	90	90
<i>β</i> [°]	90	101.668(2)	90	102.913(4)
<i>γ</i> [°]	90	98.957(2)	90	90
<i>V</i> [Å ³]	2171.9(10)	1397.86(8)	11263(4)	1590.0(9)
<i>Z</i>	4	2	16	4
<i>d</i> _{calcd.} [g/cm ³]	1.753	2.069	2.137	1.913
μ [mm ^{−1}]	4.493	6.870	8.317	6.096
GOF on <i>F</i> ²	1.059	1.010	1.029	1.177
<i>R</i> indices [<i>I</i> > 2σ(<i>I</i>)]	<i>RI</i> = 0.0340 <i>wR</i> ₂ = 0.0665	<i>RI</i> = 0.0299 <i>wR</i> ₂ = 0.0561	<i>RI</i> = 0.0508 <i>wR</i> ₂ = 0.1103	<i>RI</i> = 0.0346 <i>wR</i> ₂ = 0.0728
<i>R</i> indices (all data)	<i>RI</i> = 0.0406 <i>wR</i> ₂ = 0.0691	<i>RI</i> = 0.0521 <i>wR</i> ₂ = 0.0635	<i>RI</i> = 0.0801 <i>wR</i> ₂ = 0.1231	<i>RI</i> = 0.0424 <i>wR</i> ₂ = 0.0798
	4-Br	5-Br	6-Br	1-L2
Formula	C ₁₇ H ₁₄ Br ₂ Fe N ₂ S	C ₂₀ H ₁₇ Br ₂ Cl ₃ FeN ₂ S	C ₁₅ H ₁₆ Br ₂ FeN ₂ S	C ₅₄ H ₅₁ N ₉ S ₄ B ₄ F ₁₆ Fe ₂
FW	494.03	639.43	472.03	1413.22
Color	red	green	green-blue	violet
Habit	needle	needle	block	parallelepiped
Size [mm]	0.29 × 0.13 × 0.10	0.13 × 0.10 × 0.07	0.24 × 0.09 × 0.04	0.4 × 0.4 × 0.2
<i>T</i> (K)	153(2)	153(2)	100(2)	153(2)
λ [Å]	0.71073	0.71073	0.71073	0.71073
Lattice	triclinic	monoclinic	orthorhombic	monoclinic
Space group	<i>P</i> $\bar{1}$	<i>P</i> 2 ₁ / <i>n</i>	<i>P</i> 2 ₁ 2 ₁ 2 ₁	<i>Pn</i>
<i>a</i> [Å]	8.0880(4)	9.8718(6)	9.3989(7)	8.2970(10)
<i>b</i> [Å]	10.2583(5)	14.6668(7)	11.9399(8)	19.867(2)
<i>c</i> [Å]	11.1872(5)	16.4285(11)	15.3156(11)	35.702(3)
<i>a</i> [°]	72.491(2)	90	90	90
<i>β</i> [°]	76.713(3)	95.639(2)	90	95.824(3)
<i>γ</i> [°]	81.492(3)	90	90	90
<i>V</i> [Å ³]	858.38(7)	2367.1(2)	1718.7(2)	5854.6(10)
<i>Z</i>	2	4	4	4
<i>d</i> _{calcd.} [g/cm ³]	1.911	1.794	1.824	1.603
μ [mm ^{−1}]	5.654	4.450	5.642	0.737
GOF on <i>F</i> ²	1.087	1.054	1.062	1.885
<i>R</i> indices [<i>I</i> > 2σ(<i>I</i>)]	<i>RI</i> = 0.0291 <i>wR</i> ₂ = 0.0634	<i>RI</i> = 0.0287 <i>wR</i> ₂ = 0.0597	<i>RI</i> = 0.0326 <i>wR</i> ₂ = 0.0609	<i>RI</i> = 0.0957 <i>wR</i> ₂ = 0.2327
<i>R</i> indices (all data)	<i>RI</i> = 0.0442 <i>wR</i> ₂ = 0.0689	<i>RI</i> = 0.0361 <i>wR</i> ₂ = 0.0630	<i>RI</i> = 0.0406 <i>wR</i> ₂ = 0.0632	<i>RI</i> = 0.1045 <i>wR</i> ₂ = 0.2353

X-ray Structures

$[(\text{HNNS})_2\text{Fe}][\text{BF}_4]_2$ (1-L2)

The structure of the bisligated species 1-L2 is shown in Figure 1. The two NNS ligands chelate the metal center in an overall pseudo-octahedral geometry without any steric repulsion. The thioether (S)CH₃ group of each NNS moiety is tilted away from the pyridyl fragment of the adjacent NNS ligand. The complex exhibits typical bonding parameters for a low-spin Fe^{II} species, including relatively short Fe–N_{py} and Fe–N_{SB} bond lengths [1.938(8) and 2.007(8) Å, respectively]. The Fe–S_{CH₃} distance is comparatively longer [2.269(3) Å] but well within the normal range for the binding of neutral sulfur donors to a low-spin iron(II) center.

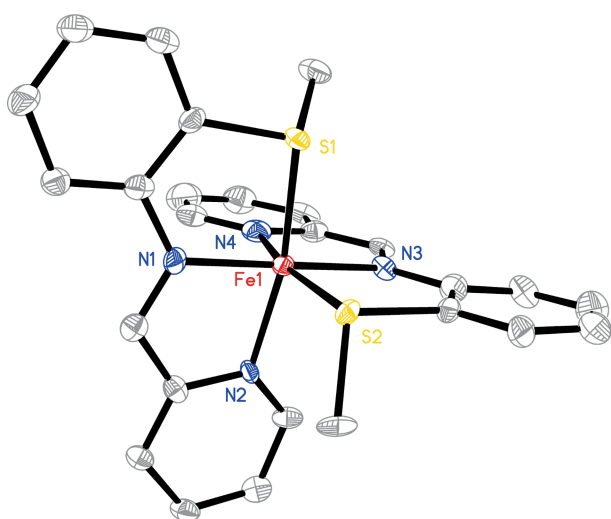


Figure 1. ORTEP diagram (50% thermal ellipsoids) of the dication of the bisligated complex 1-L2. Hydrogen atoms and counterions are omitted for clarity.

$[(\text{Me}_2\text{NNS})\text{Fe}(\text{CO})_2\text{Br}]\text{Br}\cdot\text{MeCN}\cdot\text{H}_2\text{O}$ (2-CO_{Br})

This complex (Figure 2) crystallizes as a cationic species with the charge balance provided by an outer-sphere bromide ion;

the crystallized complex is an MeCN·H₂O solvate, which indicates the stability of the carbonyl ligands in the presence of these solvents under the crystallization conditions (aerobic, dark, hydrated MeCN, –20 °C). The iron center exhibits a pseudo-octahedral geometry, and two carbonyl ligands are bound in *cis* fashion (the more commonly observed orientation). In addition, the neutral NNS chelate binds in equatorial fashion, and the remaining coordination site is occupied by one bromide ligand. The Fe–N_{py} bond length [2.039(3) Å] is longer than those typically

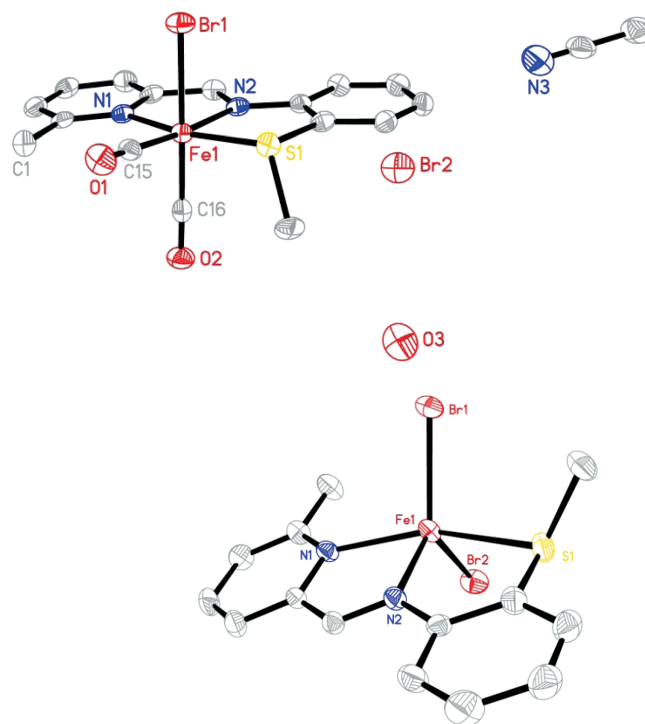


Figure 2. ORTEP diagrams (50% thermal ellipsoids) of Me₂NNS complexes. Top: 2-CO_{Br}. Bottom: 2-Br. Hydrogen atoms are omitted for clarity.

Table 2. Selected bond lengths [Å] and angles [°] derived from the X-ray structures of the dicarbonyl, dibromide, and bisligated complexes.

	2-CO _{Br}	3-CO _{Fe}	5-CO _{Fe}	2-Br	4-Br	5-Br	6-Br	1-L2
R ¹ , R ²	CH ₃ , H	OCH ₃ , H	CPh, H	CH ₃ , H	Q, H	CPh, H	H, CH ₃	H, H
Fe–N _{py}	2.039(3)	2.013(2)	2.017(10)	2.200(3)	2.196(2)	2.2376(19)	2.166(3)	1.938(8)
Fe–N _{SB}	1.957(3)	1.955(3)	1.956(10)	2.153(3)	2.133(2)	2.1262(19)	2.126(3)	2.007(8)
Fe–S _{Me}	2.2675(11)	2.2489(8)	2.257(4)	2.5519(12)	2.5758(8)	2.5793(7)	2.5696(11)	2.269(3)
Fe–Br	2.4618(8)	2.4546(6)	2.443(2)	2.4665(8)	2.5023(5)	2.4576(4)	2.4103(7)	–
Fe–C(O)	1.819(4)	1.826(3)	1.836(13)	–	–	–	–	–
<i>trans</i> SB (Fe)C–O	1.138(4)	1.129(4)	1.115(16)	–	–	–	–	–
<i>trans</i> SB (Fe)C–O	1.801(4)	1.801(4)	1.816(14)	–	–	–	–	–
<i>trans</i> Br (Fe)C–O	1.128(4)	1.130(4)	1.108(16)	–	–	–	–	–
<i>trans</i> Br R ¹ ...C(O) _{SB}	ca. 2.61	ca. 2.63	ca. 2.90	–	–	–	–	–

found for Fe–N_{py} bonds in low-spin Fe^{II} complexes, most likely because of the steric effect of the 2-methylpyridine moiety, which prevents the complete approach of the ligand to the metal center. The Fe–N_{SB} [1.957(3) Å] and Fe–S [2.2675(11) Å] bond lengths appear unaffected by the methylpyridine unit and are within the expected range for a low-spin Fe^{II} ion. The axial and equatorial carbonyl ligands exhibit distinct metric parameters [Fe–C(O) = 1.801(4), 1.819(4) Å; C–O = 1.128(4), 1.138(4) Å] owing to the different charges of the *trans* ligands (Br[−] vs. neutral N_{py}). One notable feature is the close contact between the pyridyl CH₃ moiety and the equatorial carbonyl ligand. The modeled pyridyl CH₃ protons (not located in the density map) suggest a CH₃⋯C(O) contact distance of ca. 2.2–2.6 Å, which is smaller than the sum of the Van der Waals radii. As a result, the Fe–N_{py} bond is elongated [2.039(3) Å] compared to those for the other *ortho* substituents owing to repulsion between the CH₃ group and the carbonyl ligand (see Table 2). The connectivity of the corresponding complex salt [(MeNNS)Fe(CO)₂Br][Fe(CO)₃(Br)₃] (**2-CO_{Fe}**) was also confirmed by a preliminary single-crystal X-ray diffraction study (Figure S1).

[(OMeNNS)Fe(CO)₂Br][Fe(CO)₃(Br)₃] (3-CO_{Fe}**)**

The structure of the 2-methoxypyridine derivative is shown in Figure 3. Like that of **2-CO_{Br}**, the structure exhibits a pseudo-octahedral geometry with an identical arrangement of the NNS, *cis*-CO, and bromide ligands. The Fe–N_{py} bond length of 2.013(2) Å in **3-CO_{Fe}** is shorter than that observed in the 2-methylpyridine derivative **2-CO_{Br}** [2.039(3) Å], as the O atom of the methoxy group is less bulky. Interestingly, the H₃CO_{py}⋯C(O) contact is still quite close (ca. 2.63 Å) and well within the sum of the Van der Waals radii for carbon and oxygen (1.7 + 1.5 = 3.2 Å). The remaining bond lengths are unremarkable and are listed in Table 2. The connectivity of the corresponding bromide salt [(OMeNNS)Fe(CO)₂Br]Br (**3-CO_{Br}**) was also confirmed by a preliminary single-crystal X-ray diffraction study (Figure S3). The analogous quinoline complex [(QNNS)Fe(CO)₂Br][Fe(CO)₃Br₃] (**4-CO_{Fe}**) also crystallized in this

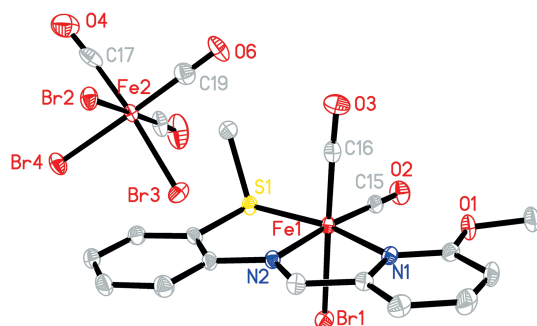


Figure 3. ORTEP diagram (50% thermal ellipsoids) of **3-CO_{Fe}**. Hydrogen atoms are omitted for clarity.

fashion, but twinning issues have precluded full structure solution at this time (see connectivity structure, Figure S4).

[(PhClNNS)Fe(CO)₂Br][Fe(Br)₄] (5-CO_{FeBr}**)**

We also prepared an NNS iron carbonyl complex bearing an aryl substituent at the pyridine *ortho* position. Owing to the higher solubility of this complex compared with those of the other complexes, the anion in the complex [(PhClNNS)Fe(CO)₂Br][Fe(CO)₃(Br)₃] (obtained initially from a reaction in Et₂O) undergoes slow oxidation under crystallization conditions (aerobic MeCN/Et₂O) to form the ferric [Fe(Br)₄][−] anion and afford the isolated complex **5-CO_{FeBr}** (Figure 4). Under an inert atmosphere, the original complex yielded crystals of low quality for X-ray structure determination (Figure S5). In the structure, the chlorophenyl group is severely rotated (dihedral angle 75.23°) to accommodate the binding of the intact (and nearly unperturbed) Fe–CO unit in the adjacent coordination position. Despite the apparent steric pressure, the Fe–N_{py} bond length [2.017(10) Å] remains comparable to those in **3-CO_{Fe}** and **4-CO_{Fe}** (see Table 2) and is much shorter than that found in proximity to the sterically impinging methylpyridine unit in **2-CO_{Br}** [Fe–N_{py} = 2.039(3) Å].

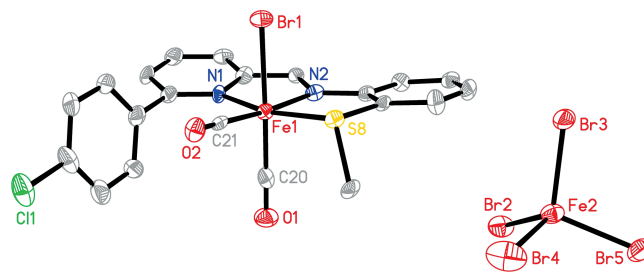


Figure 4. ORTEP diagram (50% thermal ellipsoids) of **5-CO_{FeBr}**. Hydrogen atoms are omitted for clarity.

[(R_nNNS)Fe(Br)₂] (2-Br**, **4-Br**, **5-Br**, and **6-Br**)**

ORTEP diagrams of the four dibromide complexes are either displayed alongside the corresponding dicarbonyl species in Figure 2 or in Figure 5. Each complex is neutral overall and exhibits a five-coordinate Fe ion bound to a mostly planar NNS ligand frame. One notable exception is the quinoline-based QNNS complex, which exhibits significant distortion of the conjugated ligand; there is a difference of 28.96° between the quinoline and arylthioether moieties (cf. a 7.53° offset in **3-CO_{Br}**). All of the bond lengths from the Fe ion to the NNS ligand (Fe–N_{py} ≈ 2.20 Å; Fe–N_{SB} ≈ 2.15 Å; Fe–S ≈ 2.65 Å) are significantly longer than those in the corresponding carbonyl complexes owing to the high-spin configuration of the iron center (vide infra). The Fe–Br bond lengths are more variable, within a narrow range from ca. 2.4 to 2.5 Å; **4-Br** exhibits the longest Fe–Br length [2.5023(5) Å], most likely because of repulsion between the infringing quinoline C–H unit and the equatorial bromide ligands. The remaining bond lengths are unremarkable (Table 2).

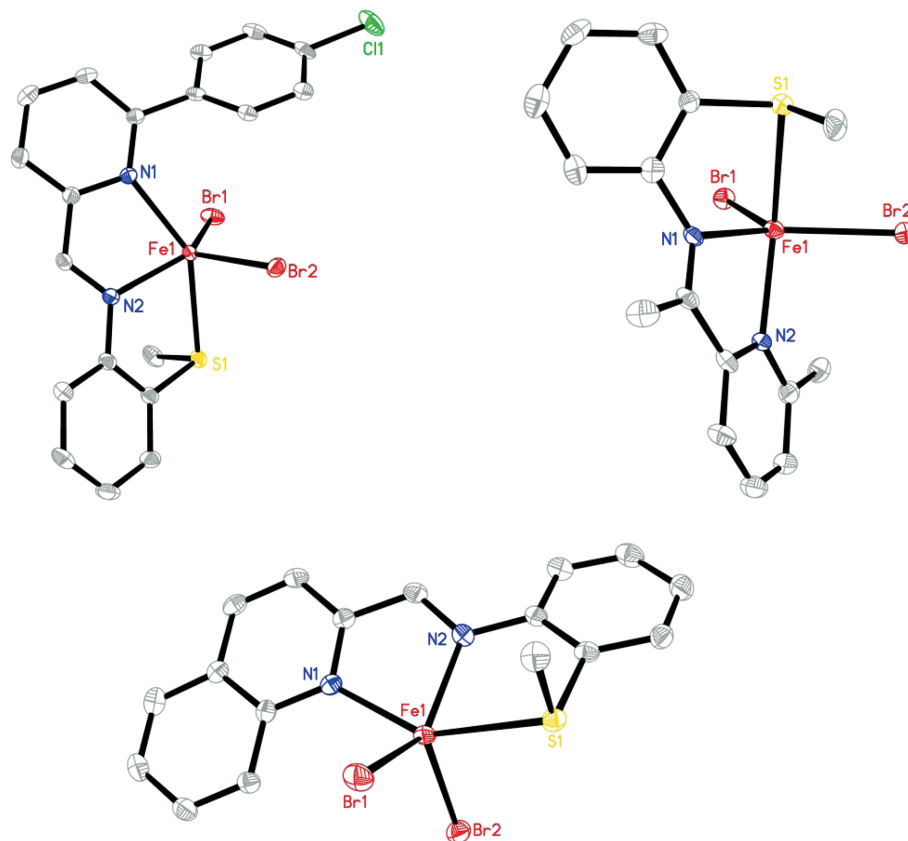


Figure 5. ORTEP diagrams (50% thermal ellipsoids) of the dibromide complexes **5-Br**, **6-Br**, and **4-Br**. Hydrogen atoms are omitted for clarity.

Characterization of the Dibromides

Magnetic Susceptibility

Solid-state magnetic measurements (298 K) on the dibromide complexes revealed a high-spin Fe^{II} center in all cases. We were unable to prepare the dibromide species derived from the unsubstituted _HNNS ligand, owing to its propensity to form only the diamagnetic bisligated species (even from FeBr₂ in THF or toluene). Considering the complexes of the aldehyde-derived ligands, **2-Br** and **4-Br** afforded both the highest and lowest μ_{eff} values of 5.48 and 5.21 μ_{B} respectively (for $S = 2$, the spin-only value, μ_{SO} , is 4.90 μ_{B}). The dibromide derived from the iminomethyl ligand, **6-Br** (no corresponding carbonyl complex was isolated), has a slightly higher value of 5.52 μ_{B} . Indeed, a notable steric clash between the iminomethyl moiety and the pyridine unit (vide supra, X-ray section) breaks the conjugation between the pyridyl and arylthioether moieties in the ligand framework. As a result, there is greater distortion

from the more ideal trigonal-bipyramidal geometries observed in **2-Br**, **4-Br**, and even **5-Br**. Thus, it is possible that the puckering of the _{Me}N_{Me}NS framework in **6-Br** contributes to its higher observed magnetic moment.

DFT Calculations for the Dibromides

To shed more light on the experimental results above, we performed DFT calculations (6-31G*/PW91) on the dibromide complexes. In each case, energy calculations with the X-ray structure coordinates were tested for both $S = 2$ and $S = 1$ configurations. The aldehyde-derived complexes **2-Br**, **4-Br**, and **5-Br** exhibited the $S = 2$ configuration as the lowest energy state by a wide margin of ca. 20 kcal/mol (20.3, 21.7, and 20.3 kcal/mol, respectively). The ketone-derived (i.e., iminomethyl) complex **6-Br** also exhibited an $S = 2$ configuration as the ground spin state but with a smaller energy difference (16.6 kcal/mol) between the $S = 2$ and $S = 1$ configurations. Overall, the DFT results are

Table 3. Properties of _RNNS Fe^{II} dibromide species.

Complex	λ [nm] (ϵ , M ⁻¹ cm ⁻¹)	Experimental		DFT	
		μ_{eff} [μ_{B}] ($S = 2$; $\mu_{\text{so}} = 4.90 \mu_{\text{B}}$)	$S = 2$ [kcal/mol]	$S = 1$ [kcal/mol]	
2-Br	460 (650)	5.48	reference (i.e., 0)	+20.3	
4-Br	460 (1180)	5.21	0	+21.7	
5-Br	460 (1570)	5.24	0	+20.3	
6-Br	460 (780)	5.52	0	+16.6	

consistent with the experimental magnetic measurements (solid state, 298 K; Table 3).

Solution Studies of the Dicarbonyl Complexes

Light/Dark Stability

The conditions under which we isolated the NNS-ligated iron dicarbonyls provided some insight into their stability in solution. For example, recrystallization at low temperatures ($-20\text{ }^{\circ}\text{C}$ or below) was required for the isolation of pure samples of each complex. Otherwise, the loss of CO led to the formation of the dibromide species. At ambient temperatures, we observed that orange solutions of the complexes in MeCN (or DMF to a lesser extent) in the dark are somewhat stable over the course of minutes to tens of minutes. The conversion to the dibromide is apparent by a distinct color change to green.

^1H NMR Spectra

The ^1H NMR spectrum of 2-CO_{Fe} in CD_3CN at $-15\text{ }^{\circ}\text{C}$ is shown in Figure 6. The aromatic resonances and multiplicities are clearly resolved, and the resonance of the Schiff base proton ($\delta = 9.68\text{ ppm}$) is shifted downfield compared to that of the free ligand ($\delta = 8.49\text{ ppm}$). In the alkyl region, the methylpyridine CH_3 group ($\delta = 3.03\text{ ppm}$) undergoes a marked downfield shift relative to that of the free ligand ($\delta = 2.46\text{ ppm}$) owing to the partial positive charge at the adjacent N_{py} atom upon binding to the Fe^{II} center. In contrast, the S-CH_3 resonance ($\delta = 2.64\text{ ppm}$) remains nearly unchanged compared to that of the free ligand ($\delta = 2.63\text{ ppm}$), as the electron density at the thioether S donor is not greatly affected in its relatively weak metal-bonding interaction.

The ^1H NMR spectra of the remaining carbonyls (2-CO to 5-CO , both Br and complex salts) all exhibit relatively sharp peaks in the diamagnetic region, consistent with an analogous low-spin Fe^{II} configuration (Figures S6–S10). In each case, orange solutions of the dicarbonyl complexes in CD_3CN turned green when equilibrated to ambient temperature, indicating the formation of the dibromide species

through the loss of CO. Thus, the ^1H NMR spectra were recorded at low temperature.

Photolysis of CO Ligands

We wished to quantitatively assess the photostabilities of this series of iron carbonyls. Measurements were standardized by using the same salt of each complex. Complexes 2-CO_{Fe} to 5-CO_{Fe} were prepared in MeCN at standard UV/Vis concentrations (ca. 0.1 mM) in quartz cuvettes, and the samples were subjected to broadband illumination from a white-light source (100 mW/cm^2). Conversion to the corresponding dibromide species (i.e., the loss of 2 equiv. of CO) was monitored by the increase in the absorption at $\lambda = 460\text{ nm}$, the characteristic absorption feature of the dibromide species. The changes in the absorption of 2-CO_{Fe} during photolysis for 50 min are shown in Figure 7. A dark control experiment (see Supporting Information, Figure S11) over the same period as that used in the photolysis experiment revealed less than 10% conversion. Of note is the decrease in the metal-to-ligand charge-transfer (MLCT) band exhibited by 2-CO_{Fe} at $\lambda \approx 380\text{ nm}$, which most likely emanates from $d_{\pi}(\text{Fe}) \rightarrow \pi^*(\text{CO})$ charge transfer. The formation of 2-Br is indicated by the increase in the broad absorption band centered at $\lambda \approx 460\text{ nm}$. We assign this band as a weak MLCT band ($\epsilon \approx 650\text{ M}^{-1}\text{cm}^{-1}$) from the Fe^{II} center to the π^* system of the ligand. The analogous changes in the UV/Vis absorption upon the photolysis of 3-CO_{Fe} , 4-CO_{Fe} , and 5-CO_{Fe} (as well as dark control experiments) are similar (Figures S12–S14).

To confirm that the changes in the UV/Vis absorption spectrum correlated with the loss of CO ligands, we monitored the reaction by solution IR spectroscopy during the photolysis. The bromide salt of the MeNNS complex, that is, 2-CO_{Br} , was used to ensure that the cation-based CO stretches of $[\text{Fe}(\text{CO})_3(\text{Br})_3]^-$ did not correlate with our UV/Vis spectroscopy observations. For comparison, the solid-state IR spectrum of 2-CO_{Br} is shown in the inset of Figure 8 (all other IR spectra are shown in Supporting Information, Figures S15–S19). As shown in Figure 8, the spectra (0–30 min) show a systematic decrease in the intensities of the CO stretches, which confirms that the changes in the

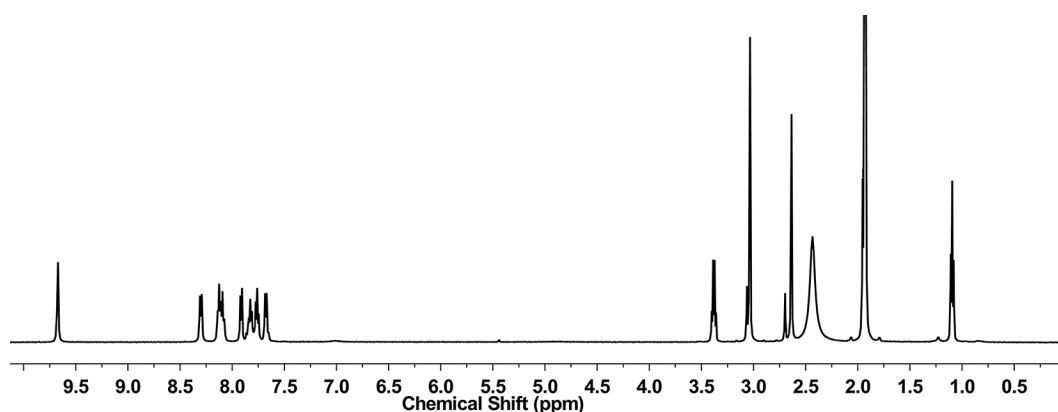


Figure 6. ^1H NMR spectrum of 2-CO_{Fe} in CD_3CN at $-25\text{ }^{\circ}\text{C}$ (500 MHz).

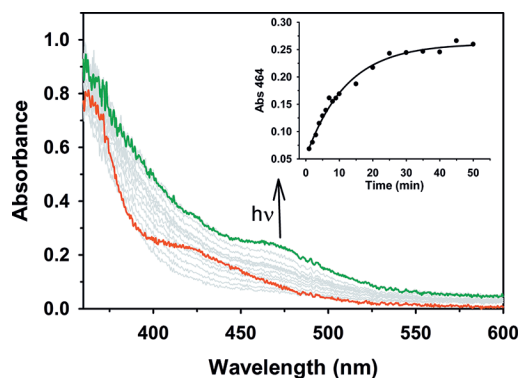


Figure 7. Changes in the UV/Vis absorption spectrum of 2-CO_{Fe} during photoconversion to the corresponding Fe^{II} dibromide 2-Br by dissociation of the CO ligands. Photolysis conditions: MeCN, 100 mW/cm^2 AM1.5 white light, 298 K.

UV/Vis spectra correlate with the loss of the CO ligands at the metal center. Note that the feature at $\tilde{\nu} = 1620\text{ cm}^{-1}$ (ligand-based C=N stretch) remains largely unchanged.

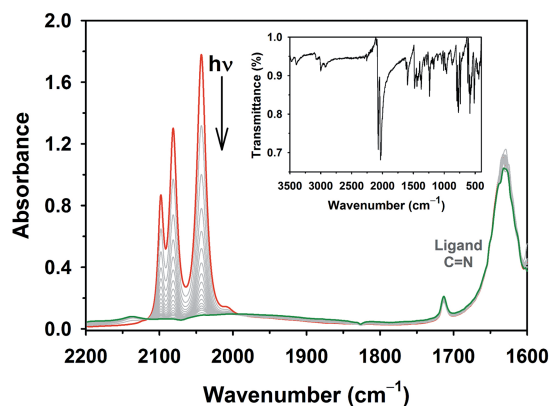


Figure 8. Solution IR spectra recorded during the photoconversion of 2-CO_{Br} to 2-Br in MeCN. Photolysis conditions: ca. 100 mM , 100 mW/cm^2 white light, 298 K. Inset: solid-state IR spectrum of 2-CO_{Br} .

The kinetic results for the photolyses of 2-CO_{Fe} to 5-CO_{Fe} are summarized in Figure 9 and Table 4. The aryl-appended 5-CO_{Fe} exhibits the fastest CO dissociation rate ($t_{1/2} = 8.5\text{ min}$), whereas the methyl- and quinoline-substituted complexes exhibit less sensitivity to light ($t_{1/2} = 12.0$ and 12.7 min). The methoxy-substituted 3-CO_{Fe} exhibits the slowest transformation to the dibromide by a wide margin ($t_{1/2} = 22.6\text{ min}$).

These results are somewhat counterintuitive in light of the structural parameters observed among the complexes. Upon first inspection, the methyl-substituted 2-CO appears to exert the greatest steric impingement upon the bound CO ligand adjacent to the *ortho* substituent. The repulsion effect between the methylpyridine and carbonyl moieties in 2-CO_{Br} is reflected in the elongated Fe-N_{py} bond length [$2.039(3)\text{ \AA}$] compared to the Fe-N_{py} bonds in the other dicarbonyl complexes (ca. $2.0\text{--}2.2\text{ \AA}$). However, this phenomenon appears to be effectively compensated by the overall shorter Fe-C(O) bond length (adjacent to the meth-

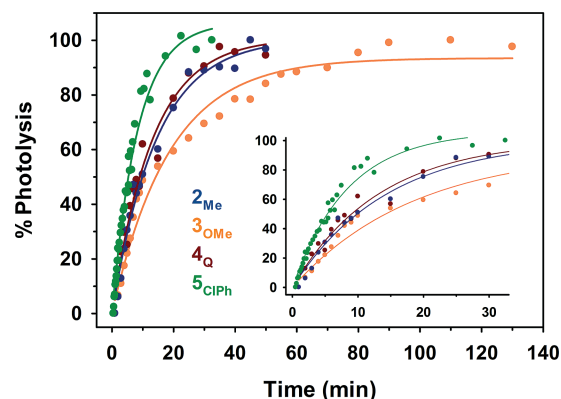


Figure 9. Photoconversion of the cationic dicarbonyl species (as indicated) to the Fe^{II} dibromides by dissociation of the CO ligands. Inset: expanded view of the same plot at short time periods. Photolysis conditions: MeCN, 100 mW/cm^2 white light, 298 K.

Table 4. Observed rates of photoconversion from the R_{NNS} cationic dicarbonyl species to the Fe^{II} dibromide species (MeCN, AM1.5 source, 100 mW/cm^2 , 298 K). Less than ca. 10% thermal conversion was observed under dark conditions over the same time period (ca. 60–120 min).

Complex	$t_{1/2}$ [min]
2-CO_{Fe}	12.0
3-CO_{Fe}	22.6
4-CO_{Fe}	12.7
5-CO_{Fe}	8.5

ylpyridine moiety, i.e., *trans* from N_{SB}) observed in 2-CO_{Br} [$1.819(4)\text{ \AA}$] compared with those in the other complexes (ca. $1.82\text{--}1.84\text{ \AA}$). Indeed, in agreement with this pattern is the correlation of the kinetically fastest transformation by 5-CO_{Fe} with the longest Fe-C(O) bond [$1.836(13)\text{ \AA}$] adjacent to the *ortho* substituent. However, the slowest $t_{1/2}$ value [3-CO_{Fe} : 22.6 min , $1.826(3)\text{ \AA}$] does not correlate with the shortest Fe-C(O) bond adjacent to the *ortho* substituent [2-CO_{Br} : $1.819(4)\text{ \AA}$]. This interpretation must be further substantiated in future work.

DFT Studies of Dicarbonyls and Photolysis Intermediates

To gain insight into the varying rates of CO photolysis, DFT and time-dependent DFT (TD-DFT) calculations were performed on the postulated photolysis intermediates. Of particular interest was the interplay between the ligand structure and the arrangement of the donors about the metal center.

Ground-State Calculations

Optimized Geometries

The synthesized complexes 2-CO and 5-CO as well as the *in silico* complex 1-CO ($\text{R} = \text{H}$) were evaluated by density functional theory. Geometry optimizations of the crystal-structure coordinates of each of these monocations proceeded smoothly at the $S = 0$ configuration. In general, the calculations afforded structures with bonding parameters

closely matched (less than $\pm 0.05 \text{ \AA}$) to those experimentally found by X-ray analysis (see Table 5). However, some trends and deviations are noted. For example, the calculated Fe–C(O)_{SB} (i.e., *trans* from the Schiff base N atom) bond lengths for **2**-CO and **5**-CO (1.779 and 1.790 \AA) are both lower than those observed in the X-ray structures [1.819(4) and 1.836(13) \AA]. The same trend is mirrored in the Fe–C(O)_{Br} distances of **2**-CO and **5**-CO, as evidenced by the shorter calculated distances of 1.761 and 1.757 \AA compared with the X-ray parameters [1.801(4) and 1.816(14) \AA]; the latter comparison is one of the greatest discrepancies (0.059 \AA) observed in the calculations. The metal–ligand bonds (i.e., the Fe–N and Fe–S bond lengths) are generally very well replicated ($\pm 0.02 \text{ \AA}$) in the DFT-calculated structures of **2**-CO and **5**-CO. The chlorophenyl-appended complex **5**-CO appears to provide the greatest differences between the calculated and experimental structures. This difference appears to be due to an inaccurate representation of the steric effect of the π electron cloud of the phenyl ring (it is underestimated) in the calculations. This is also indicated by a slightly decreased extent of linearity along the *ortho*-pyridine–chlorophenyl axis in the calculated structure ($C_{o\text{-py}}\text{--}C_{Ar}\text{--}C_{Cl} = 176.98^\circ$) with respect to that in the X-ray structure ($C_{o\text{-py}}\text{--}C_{Ar}\text{--}C_{Cl} = 178.14^\circ$). Overall, we conclude that the DFT-optimized structures are representative of the experiment results, and that the DFT calculations generate an accurate structure for the putative complex **1**-CO (with no *ortho* substituent, R = H).

Table 5. Comparisons of the experimental (**2** and **5**) and DFT-calculated (**1**, **2**, and **5**) bond lengths [\AA], bond angles [$^\circ$], and IR bands [cm^{-1}] for three NNS iron dicarbonyl complexes.

Complex	1 -CO DFT	2 -CO _{Br} X-ray	2 -CO DFT	5 -CO _{Fe} X-ray	5 -CO DFT
R ₁ , R ₂	H, H	CH ₃ , H	CH ₃ , H	ClPh, H	ClPh, H
Fe–N _{py}	1.975	2.039(3)	2.026	2.017(10)	2.011
Fe–N _{SB}	1.976	1.957(3)	1.976	1.956(10)	1.972
Fe–S _{Me}	2.283	2.2675(11)	2.287	2.257(4)	2.285
Fe–Br	2.442	2.4618(8)	2.443	2.443(2)	2.449
Fe–C(O)	1.778	1.819(4)	1.779	1.836(13)	1.790
<i>trans</i> SB (Fe)C–O	1.160	1.138(4)	1.161	1.115(16)	1.160
<i>trans</i> SB Fe–C(O)	1.763	1.801(4)	1.761	1.816(14)	1.757
<i>trans</i> Br (Fe)C–O	1.163	1.128(4)	1.164	1.108(16)	1.165
<i>trans</i> Br R ₁ ...C(O) _{SB}	ca. 2.60	ca. 2.61	ca. 2.60	ca. 2.90	ca. 2.90
$\nu(\text{CO})_1$	2056 (sym)	2069	2050 (sym)	2070	2052 (sym)
$\nu(\text{CO})_2$	2014 (asym)	2032	2009 (asym)	2025	2005 (asym)

Hessian calculation and IR frequencies

To confirm a true energy minimum for each complex, Hessian calculations were performed. All of the optimized geometries for **1**-CO, **2**-CO, and **5**-CO afforded Hessian outcomes with no negative frequencies. The calculated $\nu(\text{CO})$ values for **2**-CO and **5**-CO are consistently $20 \pm 3 \text{ cm}^{-1}$ lower than the experimental values. For exam-

ple, the calculated symmetric stretch of $\tilde{\nu} = 2050 \text{ cm}^{-1}$ for **2**-CO is lower than the experimentally observed stretch at $\tilde{\nu} = 2069 \text{ cm}^{-1}$ in the solid-state IR spectrum of **2**-CO. In another case, the calculated asymmetric stretch for **5**-CO was 2005 cm^{-1} , whereas the experimentally observed lowest $\nu(\text{CO})$ stretch was at $\tilde{\nu} = 2025 \text{ cm}^{-1}$ [solid state, attenuated total reflectance (ATR) IR]. This supports a high level of confidence (considering the $+20 \pm 3 \text{ cm}^{-1}$ correction from the DFT to experimental values)^[24] for the predicted IR stretches of the *in silico* complex **1**-CO.

TD-DFT and UV/Vis Absorption Calculations

It is first noted that the experimentally observed UV/Vis spectra for **2**-CO to **5**-CO exhibit very little variance, which is notable for the wide range of R groups [small and large, electron-donating (ED) and electron-withdrawing (EW)] implemented in the present work. This clearly suggests that the electronic environment that leads to the $d_{\pi}(\text{Fe}) \rightarrow \pi^*(\text{CO})$ MLCT (vide infra) is not greatly affected by the ligand substituents. For example, **2**-CO, **3**-CO, and **5**-CO exhibit λ_{max} in the near-UV at $425 \pm 5 \text{ nm}$. The only exception to this trend is the quinoline-derived complex **4**-CO, which exhibits a slightly redshifted $\lambda_{\text{max}} = 435 \text{ nm}$. It is of note that **4**-CO is neither on the high side nor the low side of the dissociation rates for CO photolysis; therefore, this minor λ_{max} shift is not correlated with any change in the kinetics. Overall, the lack of substituent effects on the MLCT band is reasonable for two reasons: (1) the neutral overall charge of the NNS framework does not provide much electron density for the substituents to modulate and (2) the *ortho* placement of the substituent incurs direct interaction of the substituent with the $\{\text{Fe}(\text{CO})_2\}^{2+}$ moiety, which likely modulates the electronic effect of the group away from its “textbook” Hammett σ value.

The calculated UV/Vis spectra for **1**-CO, **2**-CO, and **5**-CO (Figure 10) continue this trend. The three calculated λ_{max} values (no correction applied) are within a narrow range from $\lambda = 386.43$ to 388.31 nm . Although the absolute values of the calculated absorption maxima are blueshifted by 40 nm, the narrow range calculated between **2**-CO and **5**-CO is consistent with the experimental results. For **1**-CO, the orbitals implicated in the transition are from an admixture transition of $[d_{\pi}(\text{Fe})]p_{\pi}(\text{Br}) \rightarrow [\sigma^*(\text{Fe}-\text{CO})_{1,2}]\sigma^*(\text{Fe}-\text{L})$ (Figure 11). Notably, the σ^* orbitals of both Fe–CO units (i.e., *trans* from Br[−] and *trans* from N_{SB}) are implicated in the destination orbital (Figure 11, right side). This is indicative that the charge-transfer band is not localized to either $\{\sigma^*(\text{Fe}-\text{CO})\}$ fragment and, thus, that the sequential photodissociation of CO must be instead governed by the structural dynamics of the excited state. It is also important to note that the originating orbital contains substantial $d_{\pi}\text{--}(\text{Fe})\pi^*(\text{CO})$ backbonding, which is the primary metal–ligand interaction that must be disrupted in the photoexcited state. The analogous calculations for **2**-CO and **5**-CO yielded similar results (Figures S20–21) with varying extents of $[\sigma^*(\text{Fe}-\text{CO})_{1,2}]\sigma^*(\text{Fe}-\text{L})$ in the destination orbital. Overall, it is clear that the absorption processes at $\lambda \approx 425 \text{ nm}$ are responsible for the CO photolysis.

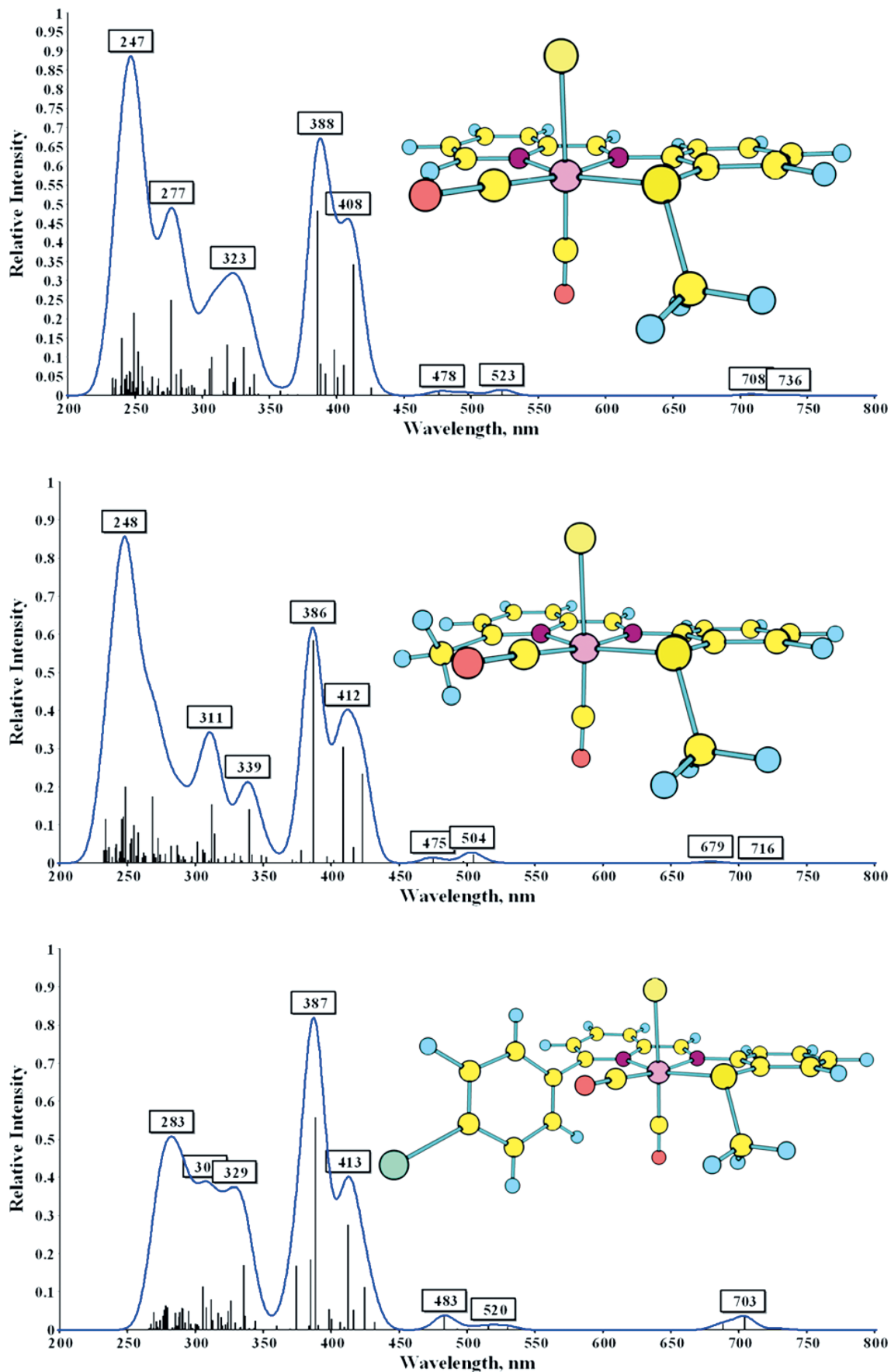


Figure 10. Calculated TD-DFT absorption spectra of 1-CO (top), 2-CO (middle), and 5-CO (bottom).

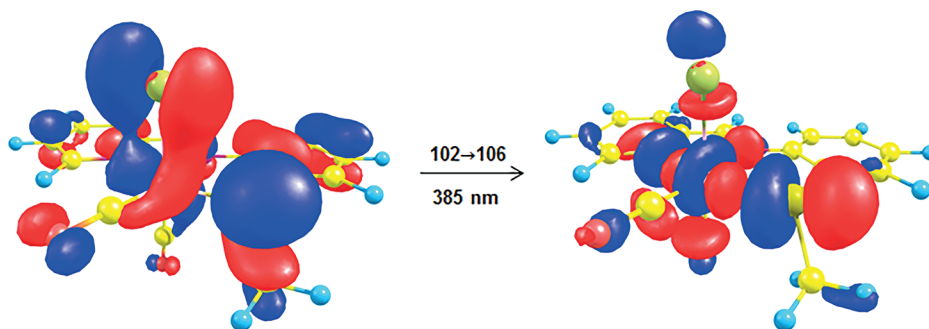


Figure 11. Molecular orbitals of **1-CO** involved in the $[d_{\pi}(\text{Fe})|p_{\pi}(\text{Br})] \rightarrow [\sigma^*(\text{Fe-CO})_{1,2}|\sigma^*(\text{Fe-L})]$ MLCT band postulated to be responsible for CO photolysis, as identified by TD-DFT calculations.

Photolysis Intermediates

One important remaining question regards the exact mechanism (or sequence) of CO dissociation that transpires during the photolysis of the dicarbonyl. To investigate this open question, we have generated DFT-optimized structures of the monocarbonyl congeners of the complexes with alternate CO ligands removed (i.e., either the CO ligand *trans* to the Br^- ion or that *trans* from N_{SB}). The results of the calculations for the unsubstituted complex (**1-CO**) are summarized in Figure 12. The *in silico* photolysis was performed, that is, the CO ligand was removed, and the energy of free $\text{C}\equiv\text{O}$ was then compensated (intermediate I_1). The removal of the axial CO ligand (*trans* to Br^-) is, not surprisingly, thermodynamically unfavorable by +34.5 kcal/mol. The DFT-optimized structure of the resulting five-coordinate monocarbonyl species remains remarkably similar to that of the dicarbonyl starting compound. This is indicated by the nearly identical angle of ca. 90° (prephotolysis: 83.00° ; postphotolysis: 88.61°) between the Br^- ligand and

the remaining equatorial carbonyl ligand. Additionally, the Fe-C(O) and $(\text{Fe})\text{C-O}$ bond lengths are only slightly modulated (by -0.004 and $+0.002$ Å, respectively) by the loss of the axial CO ligand.

By comparison, the removal of the equatorial CO ligand (*trans* to N_{SB}) results in a geometry-optimized complex (intermediate II_1) that is quite different to that for the simple removal of the CO_{eq} ligand. First, the loss of CO_{eq} is less thermodynamically unfavorable (only +22.1 kcal/mol) than the removal of CO_{ax} (+34.5 kcal/mol). Second, the remaining CO_{ax} ligand remains in essentially the same position, although the Fe-C(O) bond is shortened by 0.06 Å. Interestingly, the formerly axial Br^- ligand shifts into the vacated pseudoequatorial position. Taken together, the two *in silico* generated intermediates clearly indicate a preference for a five-coordinate monocarbonyl in which the three NNS donor atoms and an exogenous ligand (CO or Br^-) comprise the equatorial ligation. Intermediate II_1 is likely lower in energy than I_1 as the CO ligand is in the apical position, which has been observed in numerous five-coordinate Fe^{II}

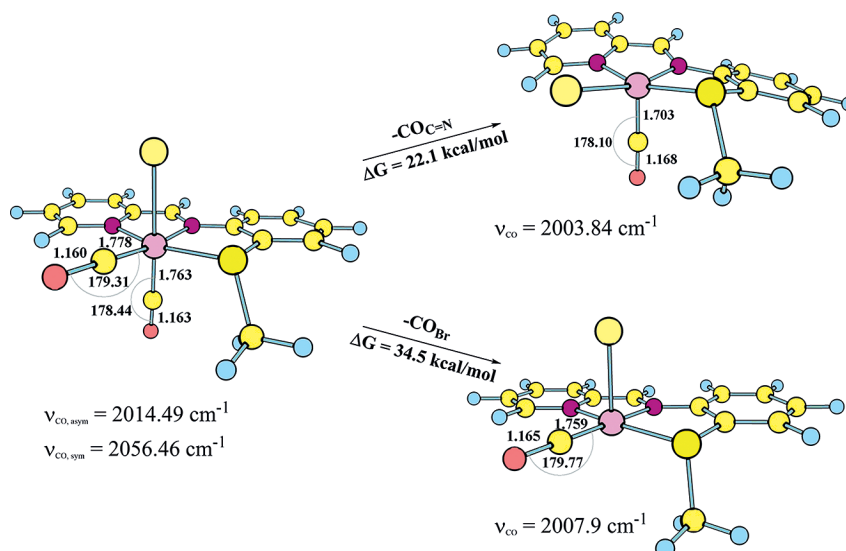


Figure 12. DFT geometry-optimized photolysis intermediates of **1-CO** generated by the removal of the axial (top) or equatorial (bottom) CO ligand. The energies were compensated for the removed $\text{C}\equiv\text{O}$ unit.

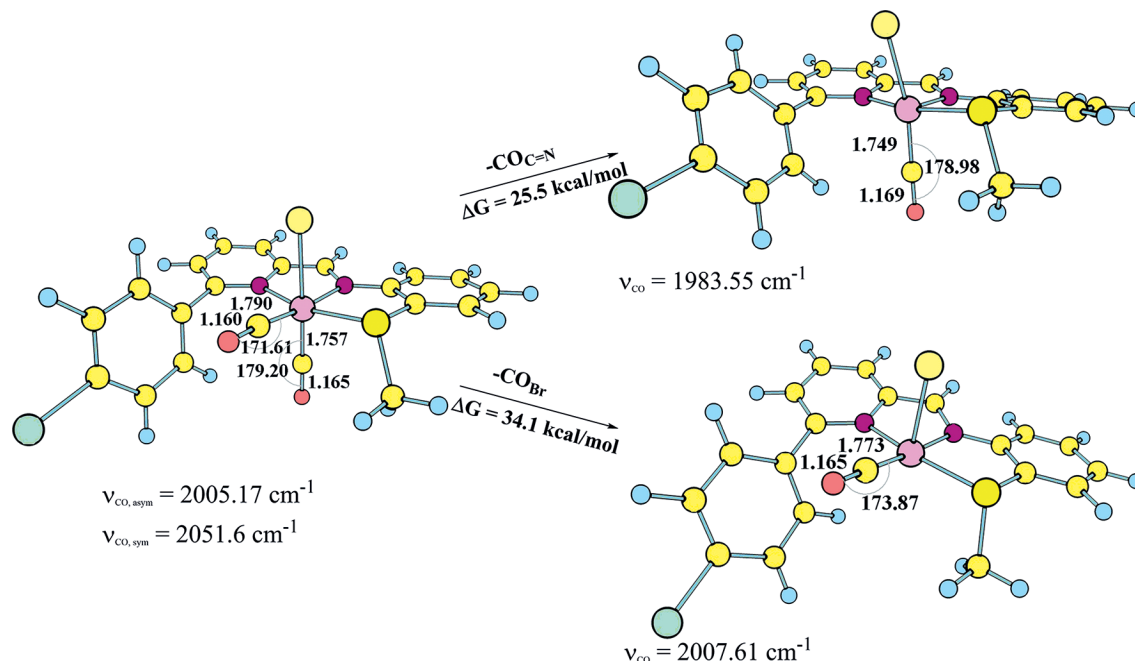


Figure 13. DFT geometry-optimized photolysis intermediates of **5-CO** generated by the removal of axial (top) or equatorial (bottom) CO ligands. The stated energies were compensated for the removed C=O unit.

and Mn^I monocarbonyls. For **2-CO** (see Supporting Information, Figure S22), an analogous pattern in I₂ and II₂ is observed for the bond-length changes (minimal), energy comparisons, and Br⁻ ligand migration upon CO_{ax} or CO_{eq} removal.

For chlorophenyl-containing **5-CO**, slightly different results were obtained (Figure 13). Although the removal of the axial CO ligand (+34.1 kcal/mol, II₅) is still more unfavorable than the loss of the equatorial CO ligand (+25.5 kcal/mol, I₅), one of the resulting intermediates is quite different (Figure 13). Chiefly, the removal of the equatorial CO ligand does not result in the migration of the Br⁻ ligand to the equatorial position. Instead, the impinging steric bulk of the chlorophenyl unit apparently prevents the downward movement of the Br⁻ ligand. This occurrence is attributed to the long Fe–Br bond [X-ray: 2.443(2) Å; DFT: 2.449 Å] and presumably the larger ionic radius of Br (1.82 Å) than that of C/O (ca. 1 Å). Overall, the following are postulated: (1) The experimental photolysis leads to the loss of the equatorial CO ligand and a driving force towards the migration of the Br⁻ ligand towards the equatorial vacancy; this affords the intermediate with the lower energy (I₁ or I₅). Then, for **5-CO**, (2) the large chlorophenyl unit in intermediate I₅ prevents the relaxation of the Br⁻ ligand into the equatorial position and, therefore, the destabilization of the structure leads to a faster loss of the second CO ligand. It may also be pointed out that the **5-CO** intermediate I₅ is the closest calculated structure to that of the actual final product of the photolysis, that is, the dibromide species **5-Br**. Experimentally, the result is an expedited CO photolysis rate for **5-CO** as compared to those for **2-CO**, **3-CO**, and **4-CO**.

Conclusions

We summarize our findings as follows:

- (1) Metalations of neutral NNS ligands with Fe^{II} carbonyl starting salts at low temperatures generally afford the desired cationic dicarbonyl species with one bromide-ligated and one outer-sphere anion.
- (2) The identity of the counteranion is determined by slight changes in the reaction conditions such as the choice of solvent (CH₂Cl₂/MeCN vs. Et₂O) or the steric demands of the ligand (R = CH₃ vs. Q).
- (3) Generally, reactions performed at temperature above –20 °C result in the loss of all CO ligands and the formation of the simple Fe^{II} dibromide species.
- (4) The resulting dicarbonyls are light-sensitive and exhibit photolysis *t*_{1/2} values (100 mW/cm²) that vary from minutes to tens of minutes depending on the concentration, counterion, and solvent conditions.
- (5) The DFT studies have revealed that the bulky chlorophenyl group destabilizes a putative photolysis intermediate (monocarbonyl I₅), a likely explanation for the rapid photolysis of **5-CO** relative to those of the other dicarbonyls.
- (6) Overall, this set of iron dicarbonyls may exhibit structural similarities to a putative apo-active site of mono-iron hydrogenase (before the formation of the acyl unit) and will provide a useful template for future studies into the biogenesis that occurs in the native enzyme.

Experimental Section

General Procedures and Reagents: All organic starting materials were purchased from Acros Organics or Sigma–Aldrich and used

without further purification. Most NNS ligands were prepared according to procedures reported by us ($\text{O}_{\text{Me}}\text{NNS}$)^[25] or others (H_2NNS , Me_2NNS , Q_2NNS)^[26–28]. The Fe^{II} starting salt $[\text{Fe}(\text{CO})_4(\text{Br})_2]$ was prepared by the reaction of $[\text{Fe}(\text{CO})_5]$ (Strem) with Br_2 according to the published procedure^[9] and purified by recrystallization from CH_2Cl_2 at -20°C instead of sublimation. HPLC grade solvents were purchased from EMD, Fisher, Macron, or J.T. Baker and dried with an alumina column system (Pure Process Technology). Deuterated solvents (CDCl_3 and CD_3CN) was purchased from Cambridge Isotopes or Acros Organics and used as received.

1-[6-(4-Chlorophenyl)pyridin-2-yl]-N-[2-(methylthio)phenyl]methanimine ($\text{C}_{19}\text{H}_{15}\text{NNS}$): 6-(4-Chlorophenyl)-2-pyridinecarbaldehyde (0.500 g, 2.30 mmol) was dissolved in MeOH (10 mL). Upon the addition of a solution of 2-methylthioaniline (0.574 g, 2.30 mmol) in MeOH (10 mL), a bright yellow hazy solution formed. The mixture was heated under reflux for 2 h, during which it turned clear. Upon cooling to room temperature, a greenish yellow precipitate was observed, and the solvent was evaporated under reduced pressure. The resulting solid was washed with Et_2O (10 mL) to remove excess 2-methylthioaniline; finally, a yellow powder was collected by filtration, yield 0.64 g (63%). Selected IR: $\tilde{\nu} = 1592$ (m), 1570 (m), 1495 (m), 1426 (m), 1317 (w), 1163 (m), 1033 (s), 930 (m), 804 (vs), 745 (vs), 677 (w), 663 (w) cm^{-1} . $^1\text{H NMR}$ (CDCl_3): $\delta = 8.67$ (s, 1 H), 8.29 (d, 1 H), 8.01 (d, 2 H), 7.89 (m, 3 H), 7.79 (d, 1 H), 7.48 (m, 2 H), 7.35 (br, 1 H), 7.12 (br, 1 H), 6.73 (1 H), 2.47 (s, 3 H) ppm. The $^1\text{H NMR}$ spectrum revealed a portion (ca. 20%) of unreacted aldehyde, which was not separated by chromatography or fractional crystallization; the ligand was thus used as prepared.

N-[1-(6-Methylpyridin-2-yl)ethylidene]-2-(methylthio)aniline (Me_2NMeNS): 2-Methylthioaniline (0.500 g, 3.69 mmol) and 2-acetyl-6-methylpyridine (0.515 g, 3.69 mmol) were dissolved separately in a minimal amount of acetic acid. The ketone was added to a round-bottomed flask, followed by the aniline. A solution of zinc chloride (0.540 g, 3.69 mmol) in acetic acid was added to the mixture and stirred. The clear, yellow-orange mixture was heated to reflux for 2 h with no color change. As the clear mixture cooled to room temperature, it became darker brown-orange, and a yellow-orange precipitate formed. The mixture was filtered, and the precipitate was washed with Et_2O . The precipitate was then dissolved in CH_2Cl_2 and extracted twice with potassium oxalate solution (to remove Zn^{2+} ions) and then twice more with distilled water. The organic layer was collected and dried with sodium sulfate, and the solvent was evaporated under reduced pressure to afford a gold-yellow oil, yield 712 mg (75%). Selected IR: $\tilde{\nu} = 1639$ (s), 1574 (s), 1460 (s), 1257 (w), 1086 (m), 1070 (m), 1036 (m), 966 (w), 733 (s) cm^{-1} . $^1\text{H NMR}$ (CDCl_3): $\delta = 8.17$ (d, 1 H), 7.61 (t, 1 H), 7.23 (m, 2 H), 7.12 (m, 2 H), 6.71 (d, 1 H), 2.61 (s, 3 H), 2.42 (s, 3 H), 2.34 (s, 3 H) ppm.

$[\text{H}_2\text{NNS}]_2\text{Fe}[\text{BF}_4]_2$ (1-L2): At room temperature, to a stirred solution of 1 equiv. of H_2NNS (100 mg, 0.438 mmol) in MeCN (10 mL) was added THF (2 mL) containing $[\text{Fe}(\text{CO})_4(\text{Br})_2]$ (118 mg, 0.438 mmol, 1 equiv.). The addition of iron(II) carbonyl immediately generated a dark violet color, which was indefinitely stable under ambient conditions. To isolate the BF_4 salt of the complex, AgBF_4 (85 mg, 0.438 mmol, 1 equiv.) in THF (2 mL) was added; although no color change was observed, a turbid solution was generated (AgBr), and the resulting mixture was stirred overnight and then filtered twice through Celite. The vapor diffusion of Et_2O at room temperature afforded violet blocks suitable for X-ray diffraction, yield 65 mg (21%). Selected IR bands: $\tilde{\nu} = 1604$ (w), 1585 (w), 1477 (m), 1306 (w), 1162 (w), 1029 (vs), 916 (m), 775 (s), 765 (s), 750 (s), 606 (m), 516 (s), 417 (w) cm^{-1} . $^1\text{H NMR}$ (500 MHz, in

CD_3CN): $\delta = 10.18$ (s, 2 H), 8.58 (d, 2 H), 8.34 (d, 2 H), 8.02 (t, 2 H), 7.82 (m, 6 H), 7.75 (t, 2 H), 7.38 (t, 2 H), 2.14 (s, 6 H) ppm. $\text{C}_{26}\text{H}_{24}\text{B}_2\text{F}_8\text{FeN}_4\text{S}_2$ (686.08); calcd. C 45.52, H 3.53, N 8.17; found C 45.29, H 3.77, N 8.27.

$[(\text{Me}_2\text{NNS})\text{Fe}(\text{CO})_2\text{Br}]\text{Br}\cdot\text{MeCN}\cdot\text{H}_2\text{O}$ (2-CO_{Br}·MeCN·H₂O): The recrystallized starting salt $[\text{Fe}(\text{CO})_4(\text{Br})_2]$ (0.150 mg, 0.457 mmol) was added to dry CH_2Cl_2 (3 mL) at -78°C in a 10 mL Schlenk flask and stirred for 5 min in the dark. The Me_2NNS ligand (0.112 g, 0.457 mmol) was dissolved in dry CH_2Cl_2 (3 mL) at -25°C and cooled to low temperature. The cold ligand solution was transferred to the $[\text{Fe}(\text{CO})_4(\text{Br})_2]$ solution at -78°C by cannulation in the dark. Stirring for 15 min in the dark afforded a dark red solution, to which was added MeCN (0.5 mL); the solution was kept at -25°C overnight. The resulting dark orange precipitate was collected by filtration and washed several times with pentane. The product was recrystallized by the slow diffusion of Et_2O into the MeCN solution at -25°C , and red crystals formed, yield 70 mg (30%). Selected IR: $\tilde{\nu} = 3011$ (w), 2069 (s), 2032 (s), 1597 (s), 1484 (s), 1469 (m), 1445 (m), 1433 (m), 1387 (m), 1376 (m), 1318 (m), 1278 (m), 1239 (m), 1174 (m), 796 (s), 770 (w), 676 (m br), 428 (m) cm^{-1} . $^1\text{H NMR}$ (500 MHz, CD_3CN , -35°C): $\delta = 9.69$ (s, 1 H), 8.29 (d, 1 H), 8.07 (d, 2 H), 7.73 (m, 4 H), 3.01 (s, 3 H, pyCH_3), 2.68 (s, 3 H, SCH_3) ppm; note: this spectrum was obtained in the presence of 1 equiv. of NaClO_4 to improve the solubility of the bromide salt (Figure S7), for the analogous spectrum in the absence of NaClO_4 , see Figure S6.

$[(\text{Me}_2\text{NNS})\text{Fe}(\text{CO})_2\text{Br}][\text{Fe}(\text{CO})_3(\text{Br})_3]$ (2-CO_{Fe}): The Me_2NNS ligand (50 mg, 0.207 mmol) in Et_2O (5 mL) was added dropwise to a clear solution of $[\text{Fe}(\text{CO})_4(\text{Br})_2]$ (67 mg, 0.207 mmol) in Et_2O (5 mL). An immediate color change to orange-green was observed along with the precipitation of the crude product. This mixture was stirred for another 30 min, after which the crude product was collected by filtration under an ambient atmosphere. The product was recrystallized by the vapor diffusion of Et_2O into a MeCN solution of the complex at -20°C to afford orange-red crystals suitable for X-ray diffraction studies (connectivity), yield 50 mg (30%). Selected IR: $\tilde{\nu} = 2092$ (m), 2075 (s), 2033 (vs), 1411 (w), 1237 (w), 798 (m), 773 (m), 621 (vs), 569 (vs), 511 (s), 442 (w) cm^{-1} . $^1\text{H NMR}$ (500 MHz, CD_3CN , -25°C): $\delta = 9.68$ (s, 1 H), 8.30 (d, 1 H), 8.09 (m, 2 H), 7.92 (d, 1 H), 7.82 (t, 1 H), 7.77 (t, 1 H), 7.67 (d, 1 H), 3.03 (s, 3 H, pyCH_3), 2.64 (s, 3 H, SCH_3) ppm (Figure 6).

$[(\text{Me}_2\text{NNS})\text{Fe}(\text{Br})_2]$ (2-Br): Method A: A solution of Me_2NNS (0.192 g, 0.0793 mmol) in dry toluene (10 mL) was added to a red solution of $[\text{Fe}(\text{CO})_4(\text{Br})_2]$ (0.260 mg, 0.0793 mmol) in dry toluene (10 mL) at room temperature. The solution quickly turned green, accompanied by vigorous gas evolution (CO gas). The reaction mixture was stirred for 30 min, and the precipitated green solid was collected by filtration under a N_2 atmosphere and dried under vacuum to give a green powder, yield 0.150 g (40%). Suitable crystals for X-ray diffraction were obtained by the vapor diffusion of Et_2O into a MeCN solution of the complex. The analytical data were consistent with those of the complex prepared by Method B.

Method B: The complex was also prepared directly from FeBr_2 in THF. Under an inert atmosphere, the Me_2NNS ligand (100 mg, 0.413 mmol) was dissolved in THF (10 mL), and to this was added THF (10 mL) containing FeBr_2 (80.0 mg, 0.371 mmol). Upon the addition of the metal salt, the solution turned dark green, and a brown precipitate formed. After stirring overnight, the THF was removed in vacuo to afford a brown solid, which was partially redissolved in CH_2Cl_2 (50 mL). This mixture was filtered, and the dark green CH_2Cl_2 solution was subjected to the vapor diffusion of Et_2O at -15°C to afford single crystals as brown blocks, yield

39 mg (23%). Selected IR: $\tilde{\nu}$ = 3011 (w), 1597 (s), 1484 (s), 1469 (m), 1445 (m), 1433 (m), 1387 (m), 1376 (m), 1318 (m), 1278 (m), 1239 (m), 1174 (m), 796 (s), 770 (w), 676 (m br), 428 (m) cm^{-1} . Solid-state magnetic susceptibility (298 K): $\mu_{\text{eff}} = 5.48 \mu_{\text{B}}$. UV/Vis (MeCN): $\lambda_{\text{max}} = 460 \text{ nm}$, $\epsilon = 650 \text{ M}^{-1} \text{cm}^{-1}$. $\text{C}_{14}\text{H}_{14}\text{Br}_2\text{FeN}_2\text{S}$ (457.99): calcd. C 36.71, H 3.08, N 6.12; found C 36.70, H 3.13, N 6.11.

[(OMeNNS)₂Fe][BF₄]₂ (3-L2): To a stirred MeCN solution (5 mL) of OMeNNS ligand (50 mg, 0.194 mmol, 1 equiv.) was added a MeCN solution (5 mL) of [Fe(H₂O)₆][BF₄]₂ (65 mg, 0.194 mmol, 1 equiv.) at room temperature. Over the course of 5 min, the solution changed from bright orange to blue-violet. The vapor diffusion of Et₂O into the MeCN solution at room temperature afforded long blue-violet needles of the product, suitable for X-ray diffraction (connectivity), yield 34 mg (23%). Selected IR: $\tilde{\nu}$ = 1607 (m), 1586 (w), 1483 (s), 1283 (s), 1045 (vs), 1030 (vs), 954 (s), 794 (s), 764 (s), 731 (s), 618 (w), 519 (w) cm^{-1} . ¹H NMR (400 MHz) in CD₃CN: δ = 11.10 (br s, 1 H), 8.65 (d, 1 H), 8.22 (d, 2 H), 8.11 (t, 1 H), 7.93 (m, 2 H), 7.74 (t, 1 H), 7.40 (br d, 1 H) ppm. $\text{C}_{28}\text{H}_{28}\text{B}_2\text{F}_8\text{FeN}_4\text{O}_2\text{S}_2$ (746.14): calcd. C 45.07, H 3.78, N 7.51; found C 45.85, H 4.07, N 7.45.

[(OMeNNS)Fe(CO)₂Br][Fe(CO)₃(Br)₃] (3-CO_{Fe}): The OMeNNS iron carbonyl complex salt was prepared according to the procedure for 2-CO_{Fe} with OMeNNS ligand (50 mg, 0.194 mmol) and iron tetracarbonyl bromide (63 mg, 0.1935 mmol). The crude precipitate was a green-orange powder. The pure complex was isolated upon recrystallization by the vapor diffusion of Et₂O into a MeCN solution of the complex at -20 °C, which afforded orange-red rod-shaped crystals suitable for single-crystal X-ray diffraction, yield 50 mg (31%). Selected IR: $\tilde{\nu}$ = 2095 (m), 2081 (m), 2032 (vs), 1593 (w), 1561 (w), 1483 (m), 1243 (w), 1192 (w), 797 (m), 572 (s), 518 (m) cm^{-1} . ¹H NMR (500 MHz, CD₃CN, -5 °C): δ = 9.66 (s, 1 H), 8.32 (br, 1 H), 8.21 (br, 1 H), 7.89 (br, 2 H), 7.82 (br, 1 H), 7.75 (t, 1 H), 7.31 (d, 1 H), 4.22 (s, 3 H), 2.64 (s, 3 H) ppm (Figure S8).

[(Q₂NNS)Fe(CO)₂Br][Fe(CO)₃(Br)₃] (4-CO_{Fe}): Surprisingly, this complex salt was prepared by same procedure (CH₂Cl₂, -78 °C) that afforded the bromide salts 2-CO_{Br} and 3-CO_{Br} (see procedure above) with Q₂NNS ligand (127 mg, 0.458 mmol) and iron tetracarbonyl dibromide (150 mg, 0.458 mmol). A small portion of Et₂O (3 mL) was layered on the reaction mixture, and storage of the solution at -25 °C afforded X-ray quality crystals of the complex salt, yield 163 mg (42%). Selected IR: $\tilde{\nu}$ = 2075 (s), 2035 (s), 2018 (s), 1606 (w), 1586 (w), 1338 (w), 1022 (w), 822 (m), 750 (m), 616 (w) cm^{-1} . ¹H NMR (500 MHz, CD₃CN, -35 °C): δ = 9.98 (s, 1 H), 8.85 (d, 1 H), 8.68 (d, 1 H), 8.39 (m, 2 H), 8.25 (m, 2 H), 8.01 (m, 2 H), 7.86 (m, 2 H), 2.78 (s, 3 H) ppm (Figure S9).

[(Q₂NNS)Fe(Br)₂] (4-Br): Method A: The dibromide complex of Q₂NNS was prepared according to the procedure above, except that the resulting CH₂Cl₂ solution was brought to room temperature and prepared by vapor diffusion with Et₂O. The solution was then cooled to -25 °C and stored at that temperature for several days. This process afforded green X-ray quality crystals of the product in low yield. The analytical data were consistent with those of the complex prepared by Method B.

Method B: The complex was also prepared from FeBr₂ in THF according to the procedure for 2-Br with Q₂NNS (100 mg, 0.359 mmol) in THF (10 mL) and FeBr₂ (70.0 mg, 0.325 mmol) in THF (10 mL); metalation afforded a dark green solution. After the evaporation of the THF, the residue was dissolved in CH₂Cl₂ (70 mL) to afford a green solution, which was subjected to the vapor diffusion of Et₂O at ambient temperature to afford X-ray quality green needles, yield 68 mg (42%). Selected IR: $\tilde{\nu}$ = 1611

(w), 1586 (w), 1508 (m), 1455 (w), 1431 (w), 1415 (w), 1378 (w), 1142 (w), 981 (m), 969 (m), 834 (s), 791 (m), 750 (s), 491 (m) cm^{-1} . Solid-state magnetic susceptibility (298 K): $\mu_{\text{eff}} = 5.21 \mu_{\text{B}}$. UV/Vis (MeCN): $\lambda_{\text{max}} = 460 \text{ nm}$, $\epsilon = 180 \text{ M}^{-1} \text{cm}^{-1}$. $\text{C}_{17}\text{H}_{14}\text{Br}_2\text{FeN}_2\text{S}$ (494.03): calcd. C 41.33, H 2.86, N 5.67; found C 40.59, H 2.94, N 5.44.

[(C₁₈H₁₈NNS)Fe(CO)₂Br][Fe(CO)₃(Br)₃] (5-CO_{Fe}): The C₁₈H₁₈NNS iron carbonyl complex salt was prepared according to the procedure for 2-CO_{Fe} with C₁₈H₁₈NNS ligand (50 mg, 0.148 mmol) and iron tetracarbonyl bromide (48 mg, 0.148 mmol). The precipitate was an orange powder, which showed an IR spectrum consistent with the formulation of the complex salt [(C₁₈H₁₈NNS)Fe(CO)₂Br][Fe(CO)₃(Br)₃]. Selected IR: $\tilde{\nu}$ = 2095 (m), 2067 (m), 2037 (s), 2025 (vs), 1600 (w), 1254 (w), 1095 (m), 966 (w), 760 (m), 621 (s), 581 (s), 437 (w) cm^{-1} . Samples of the complex as both the [Fe(CO)₃(Br)₃]⁻ salt (main product) and [Fe(Br)₄]⁻ salt (minor product) were obtained upon recrystallization by the vapor diffusion of Et₂O into an MeCN solution of the complex at -20 °C over an extended period (1–2 weeks); this afforded very small, thermally unstable and extremely light-sensitive orange crystals suitable for synchrotron X-ray diffraction, yield 43 mg (48%). Selected IR: $\tilde{\nu}$ = 2092 (m), 2070 (m), 2033 (s), 2025 (s), 1614 (w), 1253 (w), 1094 (m), 967 (m), 768 (m), 619 (m), 580 (s), 439 (w) cm^{-1} . ¹H NMR (500 MHz, CD₃CN, 5 °C): δ = 9.79 (s, 1 H), 8.34 (m, 2 H), 8.27 (br, 1 H), 7.86 (m, 2 H), 7.75 (m, 4 H), 7.58 (d, 1 H), 7.53 (d, 1 H), 2.54 (s 3 H) ppm (Figure S10).

[(C₁₈H₁₈NNS)Fe(Br)₂] (5-C₁₈H₁₈-Br): Method A: A solution of C₁₈H₁₈NNS (50 mg, 0.148 mmol) in dry CH₂Cl₂ (3 mL) under a N₂ atmosphere was transferred by cannulation into a solution of [Fe(CO)₄(Br)₄] (48 mg, 0.148 mmol) in dry CH₂Cl₂ and held at -78 °C. The reaction mixture changed from red to orange upon the addition of the ligand. Next, a small volume of MeCN (3 mL) was added by cannulation, and the mixture changed to red-orange. The resulting mixture was then stored at -20 °C for several days to afford a small amount of green crystals suitable for X-ray diffraction. The analytical data obtained were consistent with those of the sample prepared by Method B.

Method B: This complex was also prepared from FeBr₂ in THF according to the procedure for 2-Br with C₁₈H₁₈NNS (100 mg, 0.295 mmol) in THF (10 mL) and FeBr₂ (57 mg, 0.264 mmol) in THF (10 mL); metalation afforded a light green solution. Upon evaporation of the THF, dissolution in CH₂Cl₂ (50 mL) afforded a green solution that was subjected to the vapor diffusion of Et₂O at -15 °C to afford X-ray quality crystals (green needles) of the product, yield 70 mg (47%). Selected IR: $\tilde{\nu}$ = 3035 (m), 1620 (m), 1598 (m), 1589 (m), 1092 (m), 832 (s), 811 (s), 767 (s), 522 (m), 475 (m) cm^{-1} . Solid-state magnetic susceptibility (298 K): $\mu_{\text{eff}} = 5.24 \mu_{\text{B}}$. UV/Vis (MeCN): $\lambda_{\text{max}} = 460 \text{ nm}$, $\epsilon = 1570 \text{ M}^{-1} \text{cm}^{-1}$. $\text{C}_{19}\text{H}_{15}\text{Br}_2\text{ClFeN}_2\text{S}$ (554.51): calcd. C 41.16, H 2.73, N 5.05; found C 40.75, H 2.69, N 4.89.

[(Me₂NMeNS)Fe(Br)₂] (6-Br): The complex was prepared from FeBr₂ in THF according to the procedure for 2-Br with Me₂NMeNS (200 mg, 0.780 mmol) in THF (10 mL) and FeBr₂ (151 mg, 0.700 mmol) in THF (10 mL); metalation afforded a dark green solution. After evaporation of the THF, the residue was dissolved in CH₂Cl₂ (30 mL) to afford a green solution, which was subjected to the vapor diffusion of pentane at ambient temperature to afford X-ray-quality green-blue crystals, yield 261 mg (79%). Selected IR: $\tilde{\nu}$ = 1589 (s), 1465 (m), 1359 (m), 1007 (w), 968 (w), 799 (s), 773 (s), 756 (s), 491 (w), 464 (w) cm^{-1} . Solid-state magnetic susceptibility (298 K): $\mu_{\text{eff}} = 5.52 \mu_{\text{B}}$. UV/Vis (MeCN): $\lambda_{\text{max}} = 460 \text{ nm}$, $\epsilon =$

780 $\text{m}^{-1}\text{cm}^{-1}$. $\text{C}_{15}\text{H}_{16}\text{Br}_2\text{FeN}_2\text{S}$ (472.02): calcd. C 38.17, H 3.42, N 5.93; found C 38.28, H 3.39, N 5.91.

Physical Measurements: The ^1H NMR spectra were collected with a Varian DirecDrive 400 MHz spectrometer, and chemical shifts were referenced to CD_3CN . The UV/Vis absorption spectra were obtained at 298 K with an Ocean Optics fiber optic system equipped with a low-intensity PX-2 pulsed xenon lamp and a USB2000-XR1-ES detector. Quantitative UV/Vis studies (ϵ values, kinetic stability) were obtained with ca. 0.1 mM solutions of the complexes in MeCN in 1 cm quartz cuvettes. Kinetic plots (photolysis of CO in MeCN) were analyzed in SigmaPlot 8.0 and fitted to the exponential equation $y = y_0 + a(1 - e^{-bx})$. The solid-state infrared spectra were recorded with a Bruker Alpha spectrometer equipped with a diamond ATR crystal. The solution IR data during the photolysis of 2-CO_{Br} were obtained with the same instrument equipped with a 0.1 cm path length cell with CaF_2 windows; the concentration was ca. 100 mM in MeCN; the spectra were plotted in absorbance mode to maintain linearity with concentration. Photolysis was achieved by the use of a Newport solar simulator equipped with a 150 W xenon lamp and an AM1.5 filter; the samples were placed ca. 10 cm from the light source to achieve 1 Sun illumination (100 mW/cm^2) with broadband white light. The solid-state magnetic susceptibilities were measured at 298 K with a Johnson Matthey Mark I instrument.

X-ray Diffraction Data Collection and Crystal-Structure Refinement: The data were collected with a Rigaku AFC12 diffractometer with a Saturn 724+ CCD or a Nonius Kappa CCD diffractometer with a Bruker AXS Apex II detector, both with a graphite monochromator with Mo-K_α radiation. Reduced temperatures were maintained with an Oxford Cryostream low-temperature device. The data reductions were performed with Rigaku Crystal Clear version 1.40.2. The structures were solved by direct methods with SIR973 and refined by full-matrix least-squares techniques on F^2 with anisotropic displacement parameters for the non-H atoms with SHELXL-97.4. The structure analysis was aided by the use of the programs PLATON985 and WinGX.6. The crystallographic data for $5\text{-CO}_{\text{FeBr}}$ were collected through the SCrALS (Service Crystallography at Advanced Light Source) program at the Small-Crystal Crystallography Beamline 11.3.1 at the Advanced Light Source (ALS), Lawrence Berkeley National Laboratory. The hydrogen atoms attached to carbon atoms were calculated in ideal positions with isotropic displacement parameters set to $1.2U_{\text{eq}}$ of the attached atom ($1.5U_{\text{eq}}$ for methyl hydrogen atoms). The data were checked for secondary extinction effects, but no corrections were necessary. The neutral atom scattering factors and the values used to calculate the linear absorption coefficient are from the International Tables for X-ray Crystallography.

CCDC-1046982 (for 2-CO_{Br}), -1046983 (for 3-CO_{Fe}), -1046984 (for 5-CO_{Fe}), -1046985 (for 2-Br), -1046986 (for 4-Br), -1046987 (for 5-Br), -1046988 (for 6-Br), and -1046989 (for 1-L2) contain the supplementary crystallographic data for this paper. These data can be obtained free of charge from The Cambridge Crystallographic Data Centre via www.ccdc.cam.ac.uk/data_request/cif.

DFT Calculations: Dibromide Complexes: Orbital calculations, spin configuration energies, and geometry optimizations of the crystal structures of the iron(II) dibromide complexes 2-Br and 3-Br to 6-Br were performed with the Firefly software package^[29] with either a combination of the 6-31G* basis set and the pure functional PW91^[30,31] or a TZV/B3PW91 basis set. The orbitals were visualized with MacMolPlt.^[32] Dicarbonyl Complexes: All geometries were optimized with the PW91 functional with Firefly 8.0.0.^[29] We used a hybrid basis set consisting of the Pople 6-

31G(d) basis set obtained from the EMSL Basis Set Exchange^[33,34] with diffuse functions on all heteroatoms and the ligating carbonyl carbon atoms. The modified basis set (m6-31G) of Mitin et al. was used for iron,^[35] and the revised basis set (r6-311G) of McGrath was used for bromine.^[36] TD-DFT and Hessian calculations were performed at the same level of theory as the optimizations. All Hessian calculations showed no imaginary frequencies, and rotations/translations showed energies of less than 5 cm^{-1} . Graphical manipulations were performed with ChemCraft.^[37]

Supporting Information (see footnote on the first page of this article): connectivity structures of alternative salts of the dicarbonyls, ^1H NMR spectra of the dicarbonyl complexes, kinetic traces of photolyses, solid-state IR spectra of the carbonyls, and additional schemes regarding the TD-DFT-calculated photolysis pathways.

Acknowledgments

The authors gratefully acknowledge Steve Sorey and Angela Spanenberg for technical assistance in acquiring low-temperature NMR spectra. For crystal data collection for $5\text{-CO}_{\text{FeBr}}$, we thank Professor Allen Oliver (Notre Dame) and Professor Jeanette Krause (University of Cincinnati) for data collection through the SCrALS (Service Crystallography at Advanced Light Source) program at the Small Crystal Crystallography Beamline 11.3.1 at the Advanced Light Source (ALS), Lawrence Berkeley National Laboratory, which is supported by the U.S. Department of Energy, Office of Energy Sciences Materials Sciences Division (DE-AC02-05CH11231). This research was supported by startup funds to M. J. R. provided by the UT Austin College of Natural Sciences, the Robert A. Welch Foundation (F-1822), and the ACS Petroleum Research Fund (53542-DN13). DFT calculations were performed with a computer purchased with funds from a Ralph Powe Junior Faculty Award to M. J. R. Support from the National Science Foundation (NSF) (NSF-REU program at UT Austin, grant number CHE-1003947) to C. J. is acknowledged.

- [1] S. Shima, R. K. Thauer, *Chem. Rec.* **2007**, *7*, 37.
- [2] J. A. Wright, P. J. Turrell, C. J. Pickett, *Organometallics* **2010**, *29*, 6146.
- [3] S. Shima, O. Pilak, S. Vogt, M. Schick, M. S. Stagni, W. Meyer-Klaucke, E. Warkentin, R. K. Thauer, U. Ermler, *Science* **2008**, *321*, 25.
- [4] T. Hiromoto, K. Ataka, O. Pilak, S. Vogt, M. S. Stagni, W. Meyer-Klaucke, E. Warkentin, R. K. Thauer, S. Shima, U. Ermler, *FEBS Lett.* **2009**, *583*, 585.
- [5] M. Schick, X. Xie, K. Ataka, J. Kahnt, U. Linne, S. Shima, *J. Am. Chem. Soc.* **2012**, *134*, 3271.
- [6] D. Chen, R. Scopelliti, X. Hu, *Angew. Chem. Int. Ed.* **2010**, *49*, 7512; *Angew. Chem.* **2010**, *122*, 7674.
- [7] L.-C. Song, Z.-J. Xie, M.-M. Wang, G.-Y. Zhao, H.-B. Song, *Inorg. Chem.* **2012**, *51*, 7466.
- [8] B. Hu, D. Chen, X. Hu, *Chem. Eur. J.* **2014**, *20*, 1.
- [9] P. J. Turrell, J. A. Wright, J. N. T. Peck, V. S. Oganessian, C. J. Pickett, *Angew. Chem. Int. Ed.* **2010**, *49*, 7508.
- [10] D. Chen, R. Scopelliti, X. Hu, *J. Am. Chem. Soc.* **2010**, *132*, 928.
- [11] X. Wang, Z. Li, X. Zeng, Q. Luo, D. J. Evans, C. J. Pickett, X. Liu, *Chem. Commun.* **2008**, 3555.
- [12] T. Liu, B. Li, C. V. Popescu, A. Bilko, L. M. Perez, M. B. Hall, M. Y. Darensbourg, *Chem. Eur. J.* **2010**, *16*, 3083.
- [13] J. M. Kuchenreuther, W. K. Myers, D. L. M. Suess, T. A. Stich, V. Pelmeshnikov, S. A. Shiigi, S. P. Cramer, J. R. Swartz, R. D. Britt, S. J. George, *Science* **2014**, *343*, 424.
- [14] S. E. McGlynn, D. W. Mulder, E. M. Shepard, J. B. Broderick, J. W. Peters, *Dalton Trans.* **2009**, 4274.

- [15] J. M. Kuchenreuther, W. K. Myers, T. A. Stich, S. J. George, Y. NejatyJahromy, J. R. Swartz, R. D. Britt, *Science* **2013**, *342*, 472.
- [16] G. Berggren, A. Adamska, C. Lambertz, T. R. Simmons, J. Es-selborn, M. Atta, S. Gambarelli, J. M. Mouesca, E. Reijerse, W. Lubitz, T. Happe, V. Artero, M. Fontecave, *Nature* **2013**, *499*, 66.
- [17] V. P. L. Velásquez, T. M. A. Jazzazi, A. Malassa, H. Görls, G. Gessner, S. H. Heinemann, M. Westerhausen, *Eur. J. Inorg. Chem.* **2012**, 1072.
- [18] W.-F. Liaw, N.-H. Lee, C.-H. Chen, C.-M. Lee, G.-H. Lee, S.-M. Peng, *J. Am. Chem. Soc.* **2000**, *122*, 488.
- [19] W.-F. Liaw, J.-H. Lee, H.-B. Gau, C.-H. Chen, S.-J. Jung, C.-H. Hung, W.-Y. Chen, C.-H. Hu, G.-H. Lee, *J. Am. Chem. Soc.* **2002**, *124*, 1680.
- [20] W.-F. Liaw, C.-H. Chen, G.-H. Lee, S.-M. Peng, *Organometallics* **1998**, *17*, 2370.
- [21] W.-F. Liaw, J.-H. Lee, H.-B. Gau, C.-H. Chen, G.-H. Lee, *Inorg. Chim. Acta* **2001**, *322*, 99.
- [22] W.-S. Hong, C.-Y. Wu, C.-S. Lee, W.-S. Hwang, M.-Y. Chiang, *J. Organomet. Chem.* **2004**, *689*, 277.
- [23] B. Li, T. Liu, C. V. Popescu, A. Bilko, M. Y. Darensbourg, *Inorg. Chem.* **2009**, *48*, 11283.
- [24] V. Jonas, W. Thiel, *J. Chem. Phys.* **1995**, *102*, 8474–8484.
- [25] S. E. A. Lumsden, G. Durgrapasrad, K. A. M. Thomas, M. J. Rose, *Dalton Trans.* **2014**, *43*, 10725–10738.
- [26] S. K. Chatterjee, S. Roy, S. K. Barman, R. C. Maji, M. M. Olmstead, A. K. Patra, *Inorg. Chem.* **2012**, *51*, 7625.
- [27] S. Roy, P. Mitra, A. K. Patra, *Inorg. Chim. Acta* **2011**, *370*, 247.
- [28] M. A. Gonzalez, S. J. Carrington, N. L. Fry, J. L. Martinez, P. K. Mascharak, *Inorg. Chem.* **2012**, *51*, 11930.
- [29] A. Granovsky, *Firefly*, v. 7.1.G: <http://classic.chem.msu.su/gran/firefly/index.html>.
- [30] J. P. Perdew, J. A. Chevary, S. H. Vosko, K. A. Jackson, M. R. Pederson, D. J. Singh, C. Fiolhais, *Phys. Rev. B* **1993**, *48*, 4978.
- [31] J. P. Perdew, J. A. Chevary, S. H. Vosko, K. A. Jackson, M. R. Pederson, D. J. Singh, C. Fiolhais, *Phys. Rev. B* **1992**, *46*, 6671.
- [32] B. M. Bode, M. S. Gordon, *J. Mol. Graphics Modell.* **1998**, *16*, 133.
- [33] D. Feller, *J. Comput. Chem.* **1996**, *17*, 1571–1586.
- [34] K. L. Schuchardt, B. T. Didier, T. Elsethagen, L. Sun, V. Gurumoorthi, J. Chase, J. Li, T. L. Windus, *J. Chem. Inf. Model.* **2007**, *47*, 1045–1052.
- [35] A. V. Mitin, J. Baker, P. J. Pulay, *J. Chem. Phys.* **2003**, *118*, 7775–7782.
- [36] M. P. McGrath, *J. Chem. Phys.* **2009**, *130*, 176101.
- [37] G. A. Zhurko, *Chemcraft*: <http://www.chemcraftprog.com>.

Received: October 22, 2014

Published Online: February 2, 2015